

Neuregulin-1/ErbB4 Signaling Regulates Visual Cortical Plasticity

Highlights

- NRG1/ErbB4 signaling shows developmental and experience-dependent regulation
- NRG1 restores excitation to deprived PV neurons to enhance cortical inhibition
- NRG1/ErbB4 signaling in PV neurons is coupled to AMPA receptor response modulation
- NRG1 treatment suppresses critical period ocular dominance plasticity in vivo

Authors

Yanjun Sun, Taruna Ikrar, Melissa F. Davis, ..., Todd C. Holmes, Sunil P. Gandhi, Xiangmin Xu

Correspondence

xiangmin.xu@uci.edu

In Brief

Sun et al. finds that NRG1/ErbB4 signaling regulates the initiation of critical period visual cortical plasticity by rapidly controlling excitatory synaptic inputs onto PV neurons and thus PV-cell-mediated cortical inhibition in response to visual deprivation.

Neuregulin-1/ErbB4 Signaling Regulates Visual Cortical Plasticity

YanJun Sun,¹ Taruna Ikrar,¹ Melissa F. Davis,² Nian Gong,³ Xiaoting Zheng,² Z. David Luo,³ Cary Lai,⁴ Lin Mei,⁵ Todd C. Holmes,⁶ Sunil P. Gandhi,² and Xiangmin Xu^{1,7,8,9,*}

¹Department of Anatomy and Neurobiology, School of Medicine, University of California, Irvine, Irvine, CA 92697-1275, USA

²Department of Neurobiology and Behavior, University of California, Irvine, Irvine, CA 92697-4550, USA

³Department of Anesthesiology and Perioperative Care, University of California, Irvine, Irvine, CA 92697-4265, USA

⁴Department of Psychological and Brain Sciences, Indiana University, Bloomington, IN 47405, USA

⁵Department of Neuroscience and Regenerative Medicine, Augusta University, Augusta, GA 30912, USA

⁶Department of Physiology and Biophysics, School of Medicine, University of California, Irvine, Irvine, CA 92697-4560, USA

⁷Department of Biomedical Engineering, University of California, Irvine, Irvine, CA 92697-2715, USA

⁸Department of Microbiology and Molecular Genetics, University of California, Irvine, Irvine, CA 92697-2715, USA

⁹Lead Contact

*Correspondence: xiangmin.xu@uci.edu

<http://dx.doi.org/10.1016/j.neuron.2016.08.033>

SUMMARY

Experience alters cortical networks through neural plasticity mechanisms. During a developmental critical period, the most dramatic consequence of occluding vision through one eye (monocular deprivation) is a rapid loss of excitatory synaptic inputs to parvalbumin-expressing (PV) inhibitory neurons in visual cortex. Subsequent cortical disinhibition by reduced PV cell activity allows for excitatory ocular dominance plasticity. However, the molecular mechanisms underlying critical period synaptic plasticity are unclear. Here we show that brief monocular deprivation during the critical period downregulates neuregulin-1(NRG1)/ErbB4 signaling in PV neurons, causing retraction of excitatory inputs to PV neurons. Exogenous NRG1 rapidly restores excitatory inputs onto deprived PV cells through downstream PKC-dependent activation and AMPA receptor exocytosis, thus enhancing PV neuronal inhibition to excitatory neurons. NRG1 treatment prevents the loss of deprived eye visual cortical responsiveness *in vivo*. Our findings reveal molecular, cellular, and circuit mechanisms of NRG1/ErbB4 in regulating the initiation of critical period visual cortical plasticity.

INTRODUCTION

Synaptic plasticity of neural circuits is a required feature of learning, memory, and similar cognitive processes. Neural circuitry in the brain is shaped by experience, most profoundly during “critical periods” in early postnatal life. Experience-dependent critical period plasticity has been extensively studied in the visual cortex (Hensch, 2005). Adjustments of excitatory and inhibitory synaptic strength are believed to be a major mechanism by which cortical networks adapt to sensory input over a range of timescales from seconds to days (D’Amour and

Froemke, 2015; Feldman, 2012; Ma et al., 2013; Maffei et al., 2010).

Changes in cortical inhibition exerted by inhibitory interneurons are essential for regulating the critical period of visual development. Recently, fast-spiking, parvalbumin-positive inhibitory neurons (referred to as PV neurons) have been identified as the initial locus for critical period cortical plasticity (Kuhlman et al., 2013). PV neurons are rapidly inhibited by visual deprivation via monocular eyelid suture during the critical period, which is attributed to a decrease in local excitatory circuit inputs onto these interneurons (Kuhlman et al., 2013). The initial and transient reduction of PV cell activity establishes the conditions necessary for the experience-dependent excitatory cortical plasticity (i.e., ocular dominance plasticity). While progress has been made to understand specific neuronal types in driving critical period plasticity, the molecular mechanisms that translate brief sensory deprivation into functional changes in circuit connections remain unresolved.

Neuregulin-1 (NRG1) is essential for the normal development of the nervous system, and signaling through its tyrosine kinase receptor ErbB4 has been implicated in synaptic plasticity associated with long-term potentiation (LTP) and GABAergic circuit development (Fazzari et al., 2010; Huang et al., 2000; Mei and Xiong, 2008; Woo et al., 2007). We tested whether NRG1/ErbB4 signaling regulates functional circuit connections of PV interneurons and excitatory neurons during the critical period of visual development. Here we show that NRG1/ErbB4 signaling rapidly controls excitatory synaptic inputs onto PV neurons and thus PV-cell-mediated cortical inhibition in response to visual deprivation. Our study establishes molecular, cellular, and circuit mechanisms of NRG1/ErbB4 in regulating the initiation of critical period visual cortical plasticity.

RESULTS

NRG1/ErbB4 Signaling in PV Neurons Is Rapidly Reduced by Visual Deprivation

To determine how sensory experience is transduced into a loss of excitatory inputs to PV interneurons, we examined

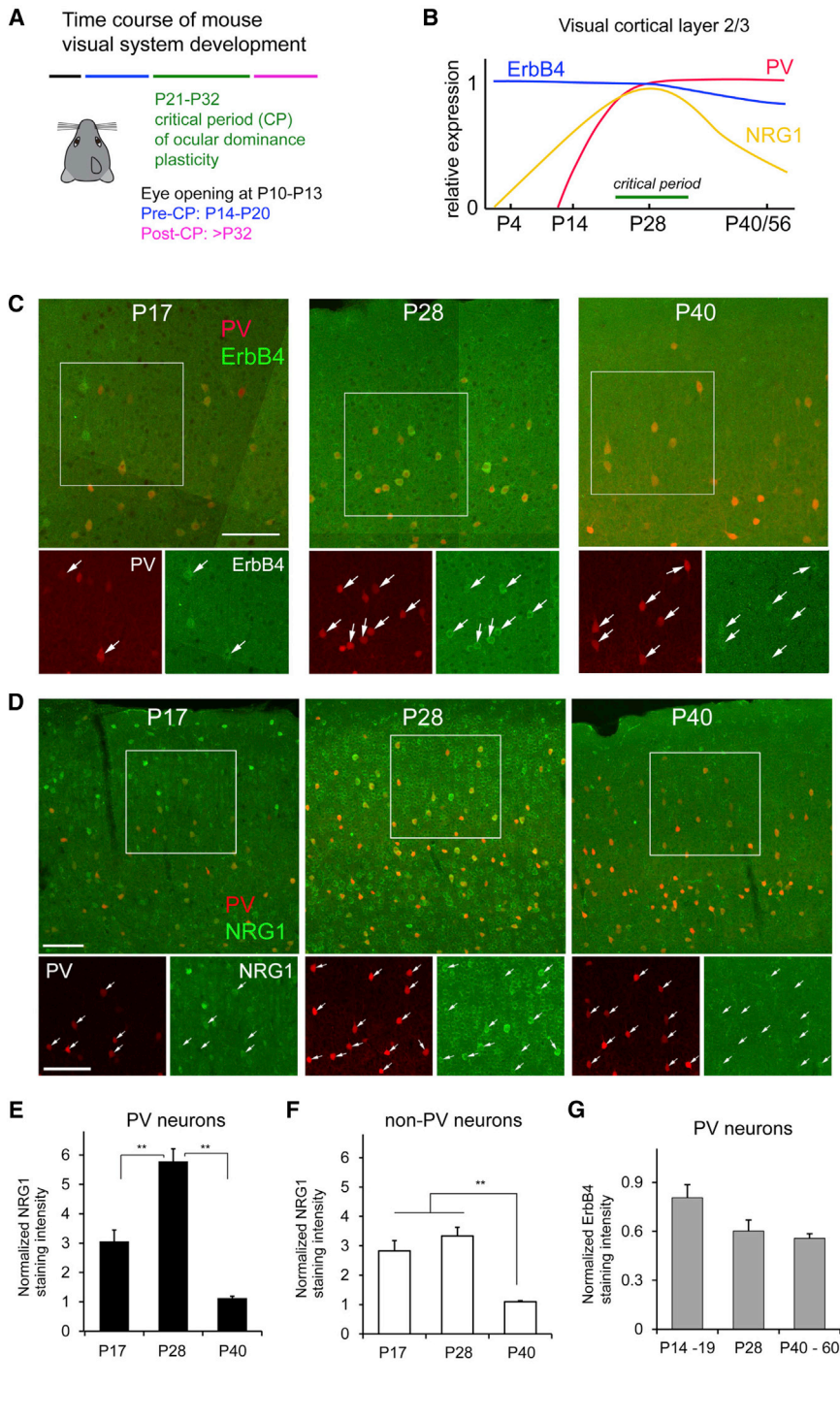


Figure 1. NRG1 and ErbB4 Expression in PV Neurons Is Developmentally Regulated

(A) The developmental times for mouse eye opening: before, during, and after the critical period (CP) for ocular dominance plasticity (Smith and Trachtenberg, 2007).

(B) A summary diagram for NRG1, ErbB4, and PV expression levels in mouse visual cortex L2/3 from postnatal days (P) 0 to P56 compared with the critical period for ocular dominance plasticity. The diagram is constructed based on our immunostaining data and in situ gene hybridization data from the Allen Brain Atlas.

(C) Representative confocal images of PV expression (red) and ErbB4 immunolabeling (green) in PV-Cre; Ai9 mouse sections of P17, P28, and P40 (dual overlap in larger top panel, detailed single-label images in smaller bottom panels).

(D) Representative confocal images show that NRG1 expression varies in PV cells in PV-Cre; Ai9 mouse V1 before (P17), at the peak of (P28), and after (P40) the critical period (dual overlap in larger top panel, detailed single-label images in smaller bottom panels). For both (C) and (D), the arrows indicate PV cells (red) and their corresponding ErbB4/NERG1 immunolabeling (green). Scale bar, 100 μ m.

(E) A bar graph shows that the average strength of NRG1 expression in PV cells varies across P17, P28, and P40, and peaks at P28. The NRG1 staining intensity at different age groups was normalized to the staining intensity of P40 in the staining series. Please see the [Experimental Procedures](#) for quantification and normalization of immunostaining intensity; the overall normalized values from different mice were compared across different age groups or conditions. PV cell measurements were obtained from five different mice for each age group. ** $p < 0.01$ (non-parametric one-way ANOVA Kruskal Wallis test, followed by Mann-Whitney U tests).

(F) A bar graph shows that average NRG1 expression of non-PV neurons is stronger in earlier ages (i.e., P17 and P28) and then decreases (P40). Non-PV cell measurements were obtained from sections of the same five mice for each age group used for PV cell measurements. ** $p < 0.01$.

(G) A bar graph shows the average ErbB4 expression strength across P14–P19, P28, and P40–P60. The ErbB4 staining intensity of PV neurons at different age groups ($n = 5, 3,$ and 3 mice, respectively) was normalized to the staining intensity of P40 in the staining series. There appears to be a trend for decreased ErbB4 expression in older ages but does not reach statistical significance (Kruskal Wallis test, $p = 0.07$). In (E)–(G), the error bar represents the standard error of the mean (SEM).

developmental expression and experience-dependent regulation of NRG1/ErbB4 signaling. We focused on layer 2/3 (L2/3) PV neurons in the binocular zone of mouse primary visual cortex (V1), where a reduction in PV cell firing rates and disinhibition of upper layer excitatory neurons occurs during the initial stage of critical period ocular dominance plasticity. To genetically label

PV neurons, we crossed PV-IRES-Cre mice (Hippenmeyer et al., 2005) with Ai9 tdTomato reporter mice (Madisen et al., 2010).

NRG1 and ErbB4 expression in PV neurons is developmentally regulated. ErbB4 expression in the visual cortex precedes PV expression (Figures 1A–1C). PV neurons show strong ErbB4

expression during the critical period of mouse visual development, as defined by ocular dominance plasticity. The ErbB4-expressing cells form a major subset of GABAergic neurons in visual cortex (Figure S1). NRG1 expression in the brain has been mapped using *in situ* hybridization (Liu et al., 2011); however, no studies have determined whether PV inhibitory neurons express NRG1. To determine this, we performed NRG1 immunostaining in visual cortical sections. PV neurons have strong and concentrated NRG1 expression revealed by immunostaining; this distinguishes them from surrounding putative excitatory neurons (Figure 1D). The stronger expression of NRG1 by PV neurons is confirmed with cell-specific fsTRAP analysis (Figure S2); the NRG1 mRNA expression in PV neurons is on average 170-fold higher as compared with excitatory neurons targeted by using *Emx1-Cre* mice. Importantly, the developmental expression of NRG1 in PV cells peaks at the critical period and correlates with the time course of critical period ocular dominance plasticity in mouse visual cortex (Figures 1A, 1B, 1D, and 1E). A great majority of PV neurons are immunopositive for NRG1. The average percentage of NRG1-expressing PV cells in L2/3 of mouse V1 is 92.5% during the critical period peak. The co-expression of the ligand NRG1 and its receptor ErbB4 in PV neurons may allow these neurons to regulate their synaptic plasticity through activity-dependent NRG1/ErbB4 signaling.

Consistent with our previous finding that firing rates of PV neurons in binocular visual cortex are rapidly inhibited with 1-day monocular deprivation (Kuhlman et al., 2013), visual deprivation reduces NRG1 expression for both mRNA (Figures 2A and 2B) and protein levels (Figures 2C and 2D) in PV neurons. Monocular deprivation also decreases the levels of activated ErbB4 (as measured by phospho-specific ErbB4 immunostaining) and overall phosphotyrosine levels in PV neurons (Figures 2C, 2D, and 2G–2I). In contrast, brief visual deprivation has no effect on NRG1 expression in putative excitatory neurons (Figure 2J). Thus, the acute and selective downregulation of NRG1 signaling in PV neurons induced by sensory deprivation is a candidate for the molecular basis of the rapid retraction of excitatory inputs to these cells and their reduced spiking activity. To further address the activity-dependent control of NRG1 expression by PV neurons, we functionally mimicked monocular deprivation effects by using Designer Receptors Exclusively Activated by Designer Drugs (DREADDs) (Sternson and Roth, 2014) to inhibit PV neuronal activity *in vivo* for 24 hr. We find that reduced PV neuronal activity evoked by 24 hr DREADDs treatment phenocopies the decreased NRG1 expression in the same targeted cells seen after 24 hr of monocular deprivation (Figures 2F and 2K). To determine whether ErbB4 activation is important for NRG1 expression in PV neurons, we acutely treated the mouse cortex with an ErbB receptor tyrosine kinase inhibitor AG1478 for less than 24 hr through intracerebroventricular injection. ErbB receptor inhibition decreases NRG1 expression in PV neurons in AG1478-treated animals (Figure 2L).

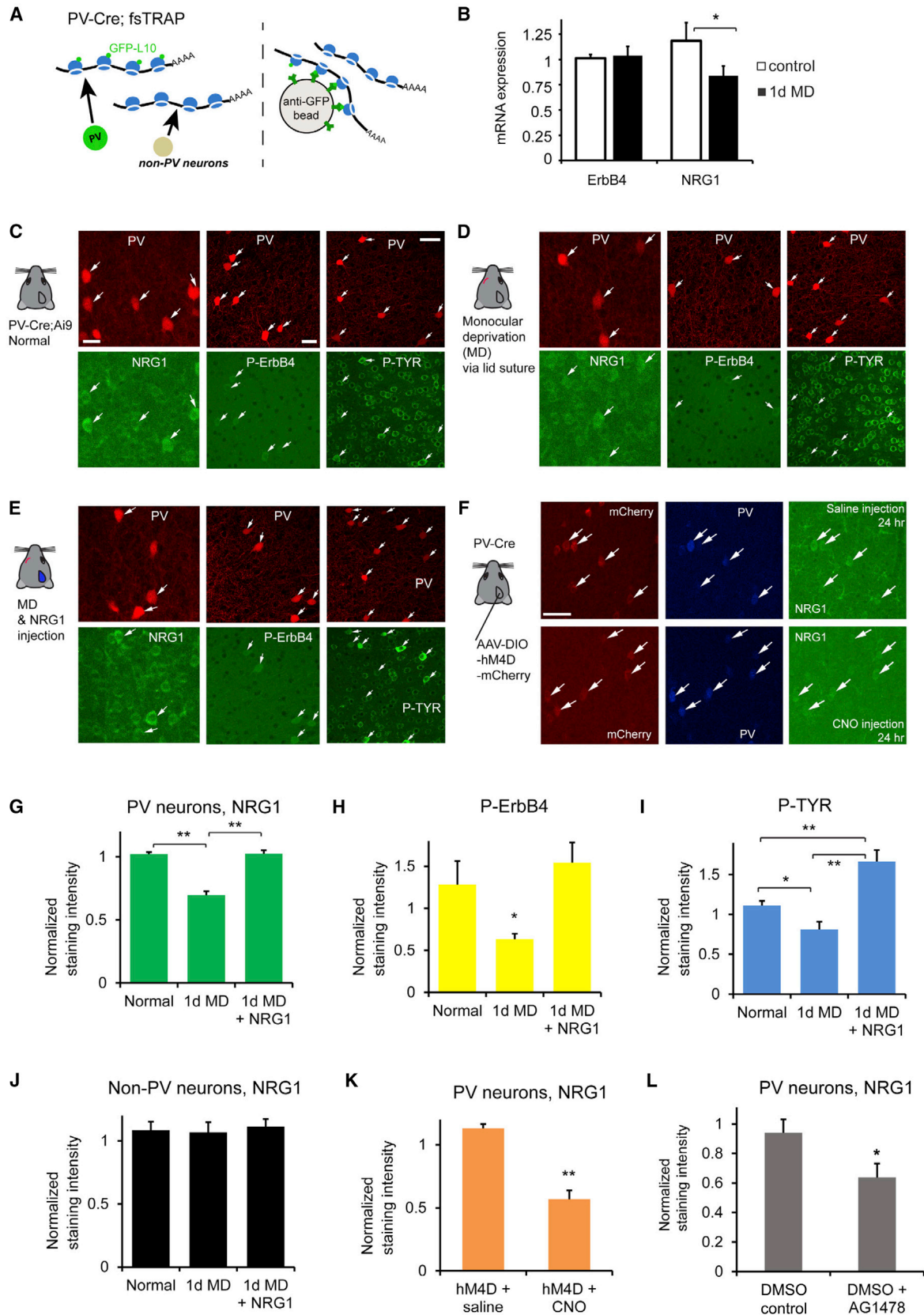
We reasoned that exogenous NRG1 treatment should reverse the physiological impact of visual deprivation on PV cells. As shown in Figure 2, NRG1/ErbB4 signaling in deprived PV cells in visual cortex is upregulated through exogenous NRG1 treatment via subcutaneous administration of recombinant NRG1 containing only the EGF core domain of NRG1- β 1. This form

of NRG1 has been shown previously to penetrate the blood-brain barrier and functionally activate ErbB4 in the cortex (Abe et al., 2011). Exogenous NRG1 treatment results in significantly increased immunostaining of NRG1 and increased phosphorylation of ErbB4 and protein tyrosine phosphorylation in PV cells in binocular visual cortex despite monocular deprivation (Figures 2E and 2G–2I). These findings indicate that systemic administration of NRG1 can be used to override the effects of monocular deprivation and independently manipulate NRG1 signaling in visual cortex to test functional outcomes *in vivo*.

Exogenous NRG1 Restores Excitatory Input to Deprived PV Neurons

To examine the causal link between decreased NRG1 signaling and the loss of excitatory inputs to PV cells, we tested the effects of NRG1 treatment on PV cell inputs following visual monocular deprivation. We predicted that enhancing NRG1 signaling would enhance excitatory inputs to deprived PV cells in L2/3 of visual cortex. We measured the connectivity strength and laminar distribution of presynaptic excitatory inputs onto L2/3 PV neurons in brain slices taken from binocular visual cortex of critical period mice (postnatal days 27–30 [P27–P30]) using laser-scanning photo stimulation (LSPS) via glutamate uncaging (Kuhlman et al., 2013; Xu et al., 2016) (Figure 3A; Figure S3). The LSPS approach is effective for detailed local circuit mapping. It involves first recording from a single neuron, then sequentially stimulating at surrounding sites to evoke action potentials from neurons in those sites through spatially restricted optically evoked glutamate release; recording from the potential postsynaptic neuron allows one to determine whether there are actual synaptic inputs from those stimulation sites. Physiological mapping experiments were performed in both normal and deprived mouse V1 slices. Normal PV neurons receive strong local excitatory inputs from L4 and upper L5 and as well as from L2/3; their inputs are dramatically reduced following 1–2 day monocular visual deprivation (Kuhlman et al., 2013) (Figures 3B and 3D).

To test our prediction that enhancing NRG1 signaling specifically enhances excitatory inputs to deprived PV cells, we examined whether enhanced NRG1 signaling restores normal excitatory drive onto these PV cells. Exogenous NRG1 treatment does not alter resting membrane potential or intrinsic membrane excitability in PV cells under normal or monocular deprivation conditions (Figure S4; Table S1); thus, intrinsic neuronal properties are not the locus for NRG1 effects. Further, acute bath application of recombinant NRG1 does not significantly modulate local excitatory synaptic inputs or direct uncaging responses of control PV neurons in binocular V1 of normal, non-lid sutured PV-Cre; Ai9 mice (Figures 3B, 3C, and 3K). This suggests that NRG1 signaling is sufficiently high to maintain synaptic input to normal PV neurons during the critical period. In contrast, bath NRG1 rapidly increases the amplitude of excitatory synaptic input to 1–2 day deprived PV cells (Figures 3D–3G and 3J; Table S2). Bath-applied NRG1 greatly potentiates direct glutamate-evoked responses as measured by responses to uncaging at perisomatic regions of PV cells. The NRG1 effects on direct responses are similar with and without the co-application of tetrodotoxin (TTX) that blocks evoked synaptic inputs (Figure 3K; Figure S5). These NRG1-enhanced responses are supported



(legend on next page)

by previous studies (Abe et al., 2011; Tamura et al., 2012) and further confirmed by the finding that NRG1 treatment increases glutamate-evoked spiking in monocular-deprived PV neurons (Figure S6). Bath NRG1 effects are robust with a fast time course (Figure 3G). The response increases are clearly detectable within 10 min and reach a plateau around 20 min following NRG1 bath application. NRG1 potentiation persists with long duration in the continued presence of the peptide, but its effects are quickly and completely eliminated within 30 min of washout.

The excitation-enhancing effects of NRG1 on deprived PV neurons are concentration dependent. We chose 5 nM bath NRG1 for slice mapping experiments based on a calibrated dose-response curve. This concentration is consistent with the physiological range of cortical NRG1 concentration (Liu et al., 2011). Desensitization of bath-applied NRG1 is not seen in recordings of longer duration; NRG1 potentiation is seen with repeated cycles of washout followed by NRG1 re-applications on the same deprived PV neurons. Thus, this indicates that NRG1 signaling strongly enhances glutamate-mediated responsiveness to restore excitatory synaptic transmission in an acute fashion rather than by initiating a long-lasting modulation process.

The effects of bath-administered NRG1 on excitatory inputs to deprived PV neurons are also observed in recordings of brain slices from animals treated with subcutaneously administered recombinant NRG1 *in vivo*. Consistent with the fast time course of bath NRG1 effects, 1-day monocular-deprived PV neurons show clear enhancement of excitatory input after 1 hr of *in vivo*

NRG1 treatment (1 μ g NRG1 per mouse, note the larger dose for this rapid acute effect *in vivo*) (Figure 3H). Exogenous *in vivo* NRG1 treatment (0.5 μ g NRG1 per mouse, three injections daily) during the duration of monocular deprivation prevents deprivation-induced excitatory input reduction in PV neurons (Figure 3I). There are temporal limits to these effects: NRG1 injection *in vivo* restricted to the first 24 hr period after eyelid suture does not prevent 48 hr-deprivation-induced excitatory input reduction (data not shown).

Consistent with the physiological changes evoked by monocular deprivation, the *in vivo* suppression of PV cell activity by DREADDs for 24 hr during the critical period causes a large reduction in local excitatory inputs (Figures 4A–4C). The DREADDs treatment inhibited PV neuronal activity for the same duration as provided by 1 day monocular deprivation. We then measured local excitatory inputs to DREADDs-inhibited PV neurons in cortical slices. As it is seen in PV neurons following brief monocular deprivation, bath NRG1 rapidly enhances excitatory synaptic inputs and direct glutamate evoked responses of DREADDs-inhibited PV cells (Figures 4D–4G). Together with the finding that reduced PV neuronal activity evoked by DREADDs leads to decreased NRG1 expression (Figures 2F and 2K), the DREADDs experiments complement our experiments with monocular deprivation and support our hypothesis that NRG1/ErbB4 signaling regulates excitatory inputs to physiologically inhibited PV neurons within the critical period.

To confirm the specificity of the effects of NRG1 on PV cells, we mapped the connectivity strength and laminar distribution

Figure 2. Monocular Deprivation Rapidly Downregulates NRG1/ErbB4 Signaling in PV Neurons of Visual Cortex during the Critical Period of Ocular Dominance Plasticity

(A and B) PV cell-specific NRG1/ErbB4 mRNA expression analysis. (A) Schematic of the translating ribosome affinity purification (TRAP) strategy (Zhou et al., 2013). Using PV-Cre; fsTRAP mice, translating polyribosomes (polysomes) from PV cells (green cells) have EGFP tags from the EGFP-L10a transgene. Lysis of all cells in the PV-Cre; fsTRAP cortex releases both tagged and nontagged polysomes. Only the tagged polysomes are captured on an anti-GFP affinity matrix and used for purification of PV-specific mRNA associated with tagged polysomes. See the [Experimental Procedures](#) and [Figure S2](#) for more information. (B) Compared to non-sutured control, 1 day of monocular deprivation (1d MD) reduces NRG1, but not ErbB4 mRNA expression in PV neurons. Each group contained six to eight samples with each sample that contained two to three visual cortex hemispheres. The y axis represents the gene expression level relative to control with the plotted values of $2^{\Delta\Delta Ct}$ (Livak and Schmittgen, 2001). * $p = 0.02$ (Mann-Whitney U test).

(C–E) Immunochemical analysis of NRG1/ErbB4 signaling. Representative images of NRG1, phospho-specific ErbB4 (P-ErbB4) and phospho-tyrosine (P-TYR) immunostaining are shown for (C) PV neurons in the PV-Cre; Ai9 mouse at postnatal day 28, (D) after 1 day of monocular deprivation (1d MD), and (E) after 1d MD with NRG1 injections (3 times [3 \times] daily, 0.5 μ g NRG1 per mouse). The image panels are contrast enhanced for the display, but not for quantitative analysis. The arrows indicate tdTomato+ PV cells (red) and their corresponding immunolabel (green). Scale bar, 20 μ m (C, left), 20 μ m (C, middle), and 40 μ m (C, right).

(F) Reduced PV neuronal activity evoked by DREADDs causes decreased NRG1 expression. Representative images of mCherry label, PV, and NRG1 immunostaining in cortical sections of PV-Cre mice with AAV-DIO-hM4D-mCherry expression in binocular V1 with saline control (top row) and clozapine N-oxide (CNO) (bottom row) *i.p.* injection for 24 hr.

(G–I) Quantitative assessment of NRG1, P-ErbB4, and P-TYR immunostaining signals in L2/3 PV cells of binocular V1 with and without 1 d MD, and 1 d MD + NRG1. A bar graph in (G) shows that the average NRG1 immunostaining signal in L2/3 PV cells significantly differs following 1 d MD but does not differ between control and 1 d MD + NRG1. PV cell measurements in (G)–(I) were obtained from four to six different mice for each condition. ** $p < 0.01$ (Kruskal Wallis test, followed by Mann-Whitney U tests). On average, 1d MD PV cells express significantly less NRG1 signal (67.9%) relative to normal control; PV cells of 1d MD occluded by NRG1 injections express similar levels of NRG1 signal relative to control. A bar graph in (H) shows average P-ErbB4 immunostaining signal in L2/3 PV cells across different conditions. PV cell measurements were obtained from sections of three to four different mice for each condition. * $p = 0.05$. On average, 1d MD PV cells express 49.5% of the P-ErbB4 signal relative to control. A bar graph in (I) shows average P-TYR immunostaining signal across different conditions. * $p \leq 0.05$ and ** $p < 0.005$. On average, 1d MD PV cells express significantly less P-TYR signal (73%) relative to control, while 1d MD PV cells treated with NRG1 injections express 150% of the P-TYR signal relative to control.

(J) The NRG1 immunostaining levels in L2/3 non-PV cells of binocular V1 do not differ across different conditions (non-PV neurons obtained from six mice each).

(K) The average NRG1 immunostaining signal in L2/3 PV cells is significantly lower in V1 cortical sections of PV-Cre mice with reduced PV neuronal activity evoked by DREADDs *in vivo* via CNO injection, compared to control saline injection (PV neuron measurements obtained from seven and five mice each). ** $p = 0.003$ (Mann-Whitney U test).

(L) Compared to control, the average NRG1 levels in L2/3 PV cells are significantly lower in the non-deprived mouse cortex treated with an ErbB receptor tyrosine kinase inhibitor AG1478 following acute intracerebroventricular delivery (<24 hr). PV neuron measurements were obtained from six mice each. * $p = 0.04$ (Mann-Whitney U test). In (B) and (G)–(L), the error bar represents the SEM.

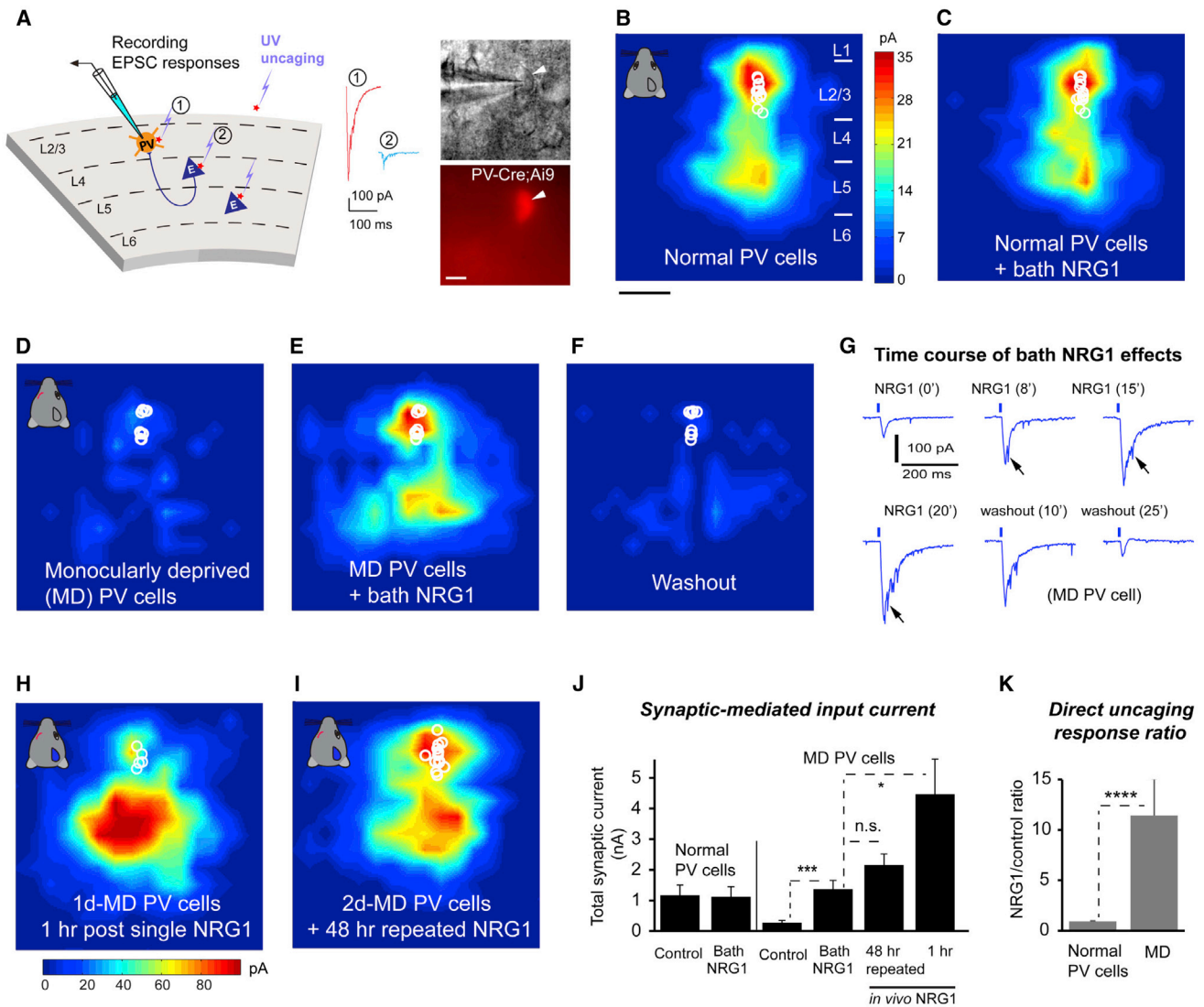


Figure 3. NRG1 Treatment Rapidly and Robustly Increases Excitatory Synaptic Input onto Monocular Deprived PV Neurons during the Critical Period

(A) Left: schematic of laser-scanning photostimulation (LSPS) mapping of local synaptic connections to individually recorded PV neurons in V1 slices. Right: targeted recordings of PV neurons are facilitated by tdTomato expression in PV-Cre; Ai9 mouse slices. Scale, 10 μ m. LSPS maps the broad spatial pattern of synaptic inputs to the neuron of interest, which distinguishes direct uncaging responses (1, red) to assess glutamate-mediated excitability/responsiveness at perisomatic locations, and synaptically mediated responses (2, cyan) to assess circuit inputs from presynaptic neuronal spiking. Cortical layers of 1, 2/3, 4, 5, and 6 in the brain slice are indicated as L1, L2/3, L4, L5, and L6.

(B and C) Acute bath application of NRG1 (5 nM) does not significantly modulate local excitatory synaptic inputs and glutamate-mediated excitability of normal PV neurons in non-deprived binocular V1 of control mice. Group-averaged, excitatory input maps of L2/3 PV cells ($n = 13$ cells) are shown for before (B) and during bath NRG1 (20 min after NRG1 application). (C) White circles represent individual PV neurons. The color scale (B) codes integrated excitatory input strength (blue = low, red = high) and applies to all other maps except (H). The spatial scale bar beneath (B) indicates 200 μ m.

(D–F) PV neurons in mice with 1–2 days of monocular lid suture show dramatically lower excitatory synaptic inputs compared to controls (D, $n = 10$ cells). However, excitatory inputs to PV neurons in these deprived mice are restored to levels above that of controls by acute bath application of NRG1 (E). This restoration is eliminated by washout of bath NRG1 (F).

(G) The fast time course of NRG1-induced potentiation of PV neuronal responses is shown for a representative neuron from a monocular deprived animal. The glutamate uncaging responses were recorded from a deprived PV neuron at a perisomatic region. Arrows indicate the enhanced magnitude of synaptic inputs superimposed on the larger waveform of the co-enhanced direct response with bath NRG1.

(H) Single in vivo NRG1 injection (subcutaneous, 1 μ g per mouse) clearly potentiates excitatory input to 1-day monocular-deprived PV cells ($n = 5$ cells) in the slices prepared 1 hr post-injection. The color scale beneath (H) codes integrated excitatory input strength. Note that compared to bath NRG1, in vivo NRG1 causes larger direct responses that mask some of the smaller synaptic inputs from perisomatic regions in L2/3. This contributes to the appearance that enhancement of excitatory inputs from deep layers by in vivo NRG1 is stronger than those from layer 2/3 (cf. E and H). However, this is probably due to the relatively larger concentration of NRG1 required for the in vivo experiments.

(legend continued on next page)

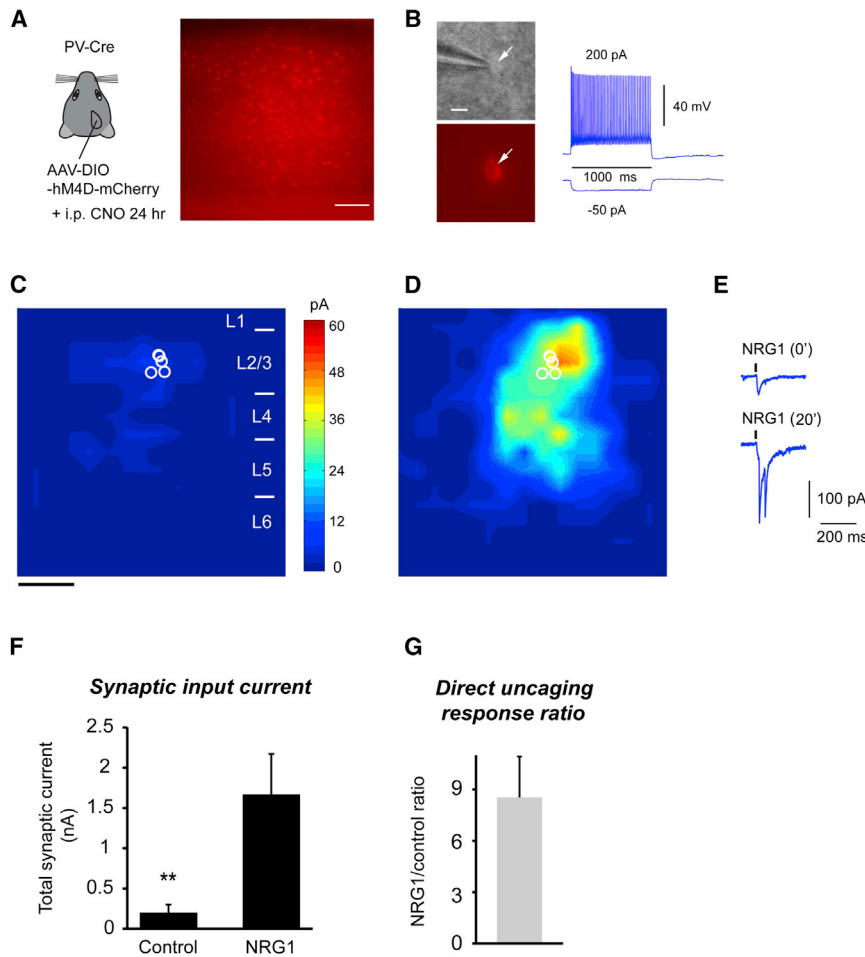


Figure 4. In Vivo Inactivation of PV Neurons by DREADDs for 24 hr Shows a Large Reduction in Local Excitatory Input, and This Is Restored by Bath NRG1 Application

(A) Use of the DREADDs to reduce PV neuron activity in vivo phenocopies the effect evoked by monocular deprivation. Left: a schematic of injecting AAV-DIO-hM4D-mCherry in binocular V1 of the PV-Cre mouse. Right: a representative slice image showing AAV label by mCherry visualization in PV neurons. Scale bar, 200 μ m.

(B) Left: targeted recordings of PV neurons are facilitated by mCherry expression in PV-Cre mouse slices. Right: in vivo CNO treatment does not affect the general fast-spiking phenotype of PV neurons in vitro. Scale bar, 10 μ m.

(C and D) Group-averaged, excitatory input maps of L2/3 PV cells inhibited by DREADDs for 24 hr ($n = 6$ cells) are shown for before (C) and during (D) bath NRG1. The spatial scale beneath (C) indicates 200 μ m.

(E) Example responses evoked by photostimulation in the same perisomatic site before and during bath NRG1.

(F) Summary data of average total synaptic input strength measured for L2/3 PV neurons before (control) and during bath NRG1. ** $p < 0.01$ (Mann-Whitney U test).

(G) Direct uncaging response ratio of DREADDs-inhibited PV cells during bath NRG1 versus before NRG1 application. In (F) and (G), the error bar represents the SEM.

of presynaptic excitatory inputs onto L2/3 excitatory pyramidal neurons in binocular visual cortex. NRG1 treatment does not modulate excitatory circuit inputs to pyramidal cells in normal or deprived animals as revealed by photostimulation mapping (Figure 5). This is consistent with the finding that ErbB4 is not expressed in excitatory neurons in visual cortex (Figure S1) (also see references Fazzari et al., 2010; Vullhorst et al., 2009). Further, NRG1 treatment has no effect on intrinsic membrane excitability in pyramidal cells from normal or deprived animals (data not shown). In addition, the intracellular blocking experiments (see below, Figure 6) further localize NRG1 effects to PV cells.

Downstream NRG1 Signaling Modulates PV Neuron Responses

NRG1-induced enhancement of the deprived PV neuron response does not require NMDA receptor activation, as the co-appli-

cation of NRG1 and an NMDA receptor antagonist, CPP (3-((R)-2-carboxypiperazin-4-yl)-propyl-1-phosphonic acid) has no effect of suppressing NRG1-enhanced PV neuronal responses (Figures 6A, 6B, 6I, and 6J). As fast excitatory synaptic currents are mediated by postsynaptic AMPA receptors in PV neurons, this result also suggests that downstream NRG1 signaling modulates AMPA receptors.

The observed enhancement of PV excitatory inputs when NRG1 is administered is specific to direct NRG1 signaling at ErbB4 receptors on PV neurons. In the presence of an acutely applied ErbB receptor tyrosine kinase inhibitor AG1478, no significant NRG1 effects are observed for deprived PV cells (Figures 6C, 6D, 6I, and 6J). In PV-Cre; ErbB4^{flx/flx} mice in which ErbB4 is ablated specifically in PV-positive interneurons (Long et al., 2003), bath NRG1 has no effect on excitatory synaptic inputs to monocular-deprived PV neurons (Figures S7A–S7C). In addition, the PV cells with ErbB4 genetic ablation show reduced excitatory inputs compared with normal, non-ErbB4 knockout

(I) 2-day NRG1 injections (0.5 μ g every 8 hr) during 2d MD in vivo prevent excitatory input reduction. Note that injecting NRG1 for only the first day of 2d MD does not prevent excitatory input reduction. Group-averaged, excitatory input maps are shown for L2/3 PV cells for 2d MD mice with 2-day NRG1 injections ($n = 10$ cells).

(J) Summary data of average total synaptic input strength measured for L2/3 PV neurons under the specified conditions. * $p = 0.03$ and *** $p = 0.001$ (Mann-Whitney U tests). The n.s. indicates no significant difference ($p = 0.2$).

(K) Direct uncaging response ratios of before and during bath NRG1 for normal versus deprived PV cells. We measured peak direct responses, which are not affected by overriding synaptic inputs. **** $p = 4.6E-05$ (Mann-Whitney U test). In (J) and (K), the error bar represents the SEM.

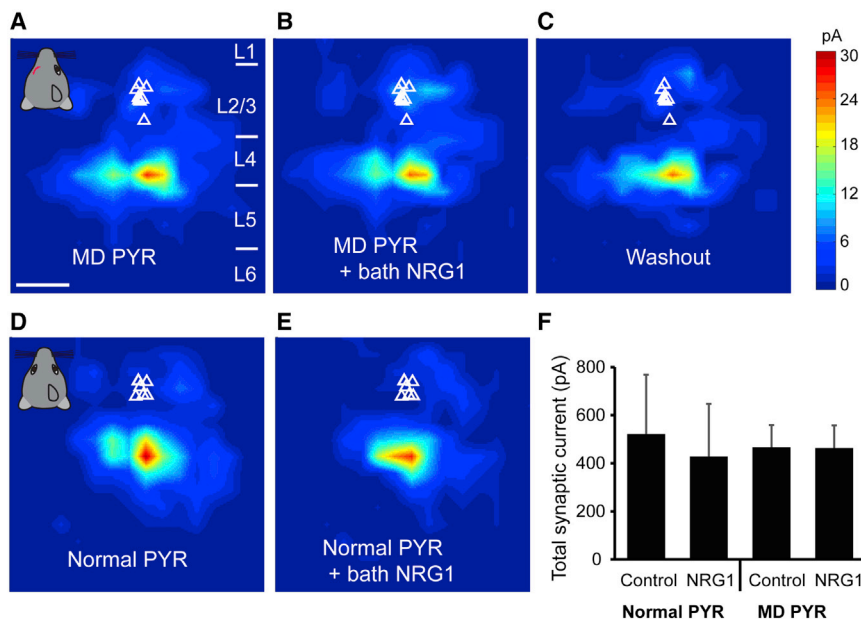


Figure 5. NRG1 Treatment Does Not Modulate Excitatory Synaptic Input onto Pyramidal Neurons under Normal or Monocular Deprivation Conditions

(A–C) Quantitative group-averaged, excitatory input maps of monocular-deprived (MD) L2/3 pyramidal (PYR) neurons are shown for before (A, $n = 9$ cells), during (20 min after NRG1 application, B), and after (C) washout of bath NRG1. White triangles represent individual pyramidal neurons. The spatial scale bar in (A) indicates 200 μm . Color scale in (C) indicates excitatory input strength. (D and E) Group-averaged, excitatory input maps of normal L2/3 pyramidal neurons are shown for before (D, $n = 6$ cells) and during (E) bath NRG1. (F) Summary data of average total synaptic input strength measured for control ($n = 6$) versus deprived ($n = 9$) L2/3 pyramidal neurons. There is no significant difference between the groups ($p > 0.5$, Mann-Whitney U tests). The error bar represents the SEM.

PV cells (Figures S7D and S7E). This result is in agreement with the previous finding that postsynaptic ErbB4 expression is important for the formation of excitatory synapses on hippocampal GABAergic interneurons (Fazzari et al., 2010).

Protein kinases are necessary for ocular dominance shifts during monocular deprivation (Berardi et al., 2003). We therefore tested whether NRG1-enhanced AMPA receptor responses by downstream NRG1/ErbB4 signaling require protein kinase C (PKC)-dependent activation. Protein phosphorylation of AMPA receptors is known to modulate AMPA receptor conductance, and the membrane trafficking and redistribution of AMPA receptors to the postsynaptic membranes (Lu et al., 2001). Canonical NRG1/ErbB signaling pathways often involve ERK and PI3K/Akt; many studies show that PI3K is an upstream regulator of protein kinase C (PKC) (Bekhitte et al., 2011; Frey et al., 2006). It is also known that the downstream signals linked to ErbB include the phospholipase C-dependent PKC pathway (Mei and Xiong, 2008). To specifically restrict the inhibition of PKC activation in recorded PV neurons, we included a pseudosubstrate non-membrane-permeable peptide inhibitor of protein kinase C (PKC 19-36) in recording glass pipettes (Chen et al., 2000) and measured the response to bath-applied NRG1. Cellular inhibition of PKC through intracellular application of the PKC inhibitor blocks NRG1-induced responses (Figures 6E, 6F, 6I, and 6J). Therefore, PKC activation is essential for NRG1/ErbB4 enhancement of AMPA receptor responses.

The timing of NRG1 potentiation of glutamate-evoked responses is consistent with the rapid insertion of the intracellular pool of AMPA receptors and increased clustering of AMPA receptors (Lu et al., 2001) at the membrane surface of PV neurons. To determine whether membrane-fusion-dependent exocytosis of internal AMPA receptors is required for the NRG1 effects on deprived PV neurons, we included botulinum toxin light chains (BTX) in the recording pipette (Li et al., 2005). BTX blocks the exocytosis of postsynaptic vesicles that contain new AMPA

receptors, thus preventing membrane insertion. Using this approach, we determined whether BTX treatment blocks the effects of bath applied NRG1. In support of our hypothesis, intracellular application of BTX prevents the NRG1-induced enhancement of glutamate responses (Figures 6G–6J). Thus, NRG1 enhancement of PV neuron excitatory inputs requires insertion of additional AMPA receptors in PV neuron postsynaptic membrane surface.

To investigate the possible requirement of protein synthesis in NRG1-enhanced PV neuronal responses, we incubated cortical slices in a protein synthesis inhibitor, anisomycin (Huber et al., 2000), before bath NRG1 experiments. Compared to control experiments, blocking new protein synthesis by the anisomycin treatment does not appear to affect the potentiation of NRG1 on excitatory inputs to deprived PV neurons (data not shown). This result indicates that acute effects of bath-administrated NRG1 do not require new protein synthesis.

NRG1 Enhances Cortical Inhibition

Previous work showed that NRG1 increases evoked GABA release and modestly enhances inhibition onto excitatory neurons in prefrontal cortex and hippocampus (Tamura et al., 2012; Wen et al., 2010; Woo et al., 2007). However, the mechanism of action of NRG1 on GABAergic neurons required further investigation. We show here that NRG1 strongly modulates evoked synaptic inhibition to pyramidal neurons in visual cortical slices, and this modulation depends both on sensory experience (i.e., monocular deprivation dependent) and ErbB4 signaling (Figures 7A–7C). Bath NRG1 increases evoked inhibitory postsynaptic currents (IPSCs) to monocular-deprived but not normal pyramidal neurons in visual cortex of wild-type mice. In addition, NRG1 has no effect on evoked IPSCs in PV-Cre; ErbB4^{flx/flx} mouse cortex.

We examined further whether NRG1 modulates PV neuron-mediated postsynaptic responsiveness in excitatory neurons or the strength of PV inhibitory output connections to excitatory

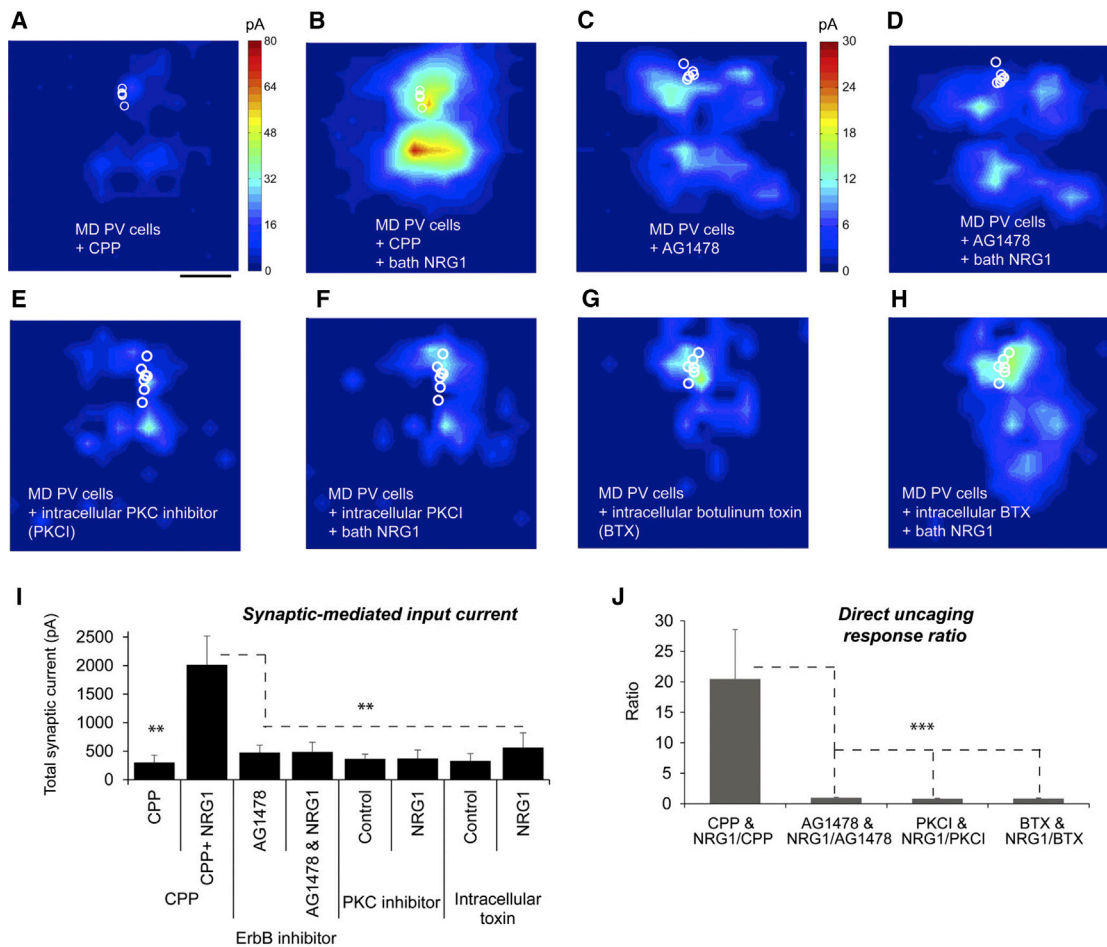


Figure 6. NRG1/ErbB4 Downstream Signaling Requires PKC-Dependent Activation and Membrane Fusion-Dependent Exocytosis of AMPA Receptors to Restore Excitatory Inputs to Deprived PV Neurons

(A and B) The NMDAR antagonist, CPP (3-((R)-2-carboxypiperazin-4-yl)-propyl-1-phosphonic acid), does not affect NRG1 potentiation of excitatory inputs of 1–2 day deprived PV neurons. Group-averaged, excitatory input maps of L2/3 PV cells ($n = 5$ cells) in the CPP presence are shown for before (A) and during (B) bath NRG1. The spatial scale beneath (A) indicates 200 μm .

(C and D) The ErbB receptor tyrosine kinase inhibitor, AG1478, blocks NRG1 effects on 1–2 day deprived PV cells. Group-averaged, excitatory input maps of L2/3 PV cells ($n = 10$ cells) in the presence of AG1478 are shown for before (C) and during (D) bath NRG1.

(E and F) Intracellular application of a pseudosubstrate peptide inhibitor of protein kinase C (PKC 19-36) prevents NRG1-induced effects on the recorded deprived PV cells. Group-averaged, excitatory input maps of L2/3 PV cells ($n = 8$ cells) in the intracellular presence of PKC 19-36 are shown for before (E) and during (F) bath NRG1.

(G and H) Intracellular application of membrane-impermeable botulinum toxin light chains (BTX) largely prevents NRG1-induced effects on the recorded deprived PV cells. Group-averaged, excitatory input maps of L2/3 PV cells ($n = 7$ cells) in the intracellular presence of BTX are shown for before (G) and during bath NRG1 (H).

(I) Summary data of average total synaptic input strength measured for L2/3 PV neurons under the specified conditions. $**p < 0.01$ (Mann-Whitney U tests). (J) Direct uncaging response ratios of before and during bath NRG1 measured for L2/3 deprived PV neurons under the specified conditions. $***p < 0.001$ (Mann-Whitney U tests). In (I) and (J), the error bar represents the SEM.

neurons by optogenetically evoking PV inhibitory inputs to pyramidal neurons (Figures 7D–7G; Figure S8). The experiments were performed in brain slices with Cre-directed channelrhodopsin-2 (ChR2) expression in PV neurons that synapse on pyramidal neurons (Madisen et al., 2012). Direct inhibitory connections to pyramidal neurons were mapped by ChR2 photoactivation of somatic spiking of presynaptic PV inhibitory neurons (Figure S8F). Bath NRG1 application does not modulate PV-specific inhibition to L2/3 pyramidal cells (Figures 7H–7K). Thus, the NRG1 increase of cortical inhibition in deprived cortex is local-

ized specifically to enhance excitatory drive to deprived PV neurons, rather than modulating PV neuron-mediated postsynaptic responsiveness or PV inhibitory synaptic connections to pyramidal cells.

Enhanced NRG1 Signaling Suppresses Cortical Plasticity

Next, we investigated the function of NRG1/ErbB4 signaling in ocular dominance plasticity in vivo. As described above and proposed in our model (Figure 8A), downregulation of NRG1

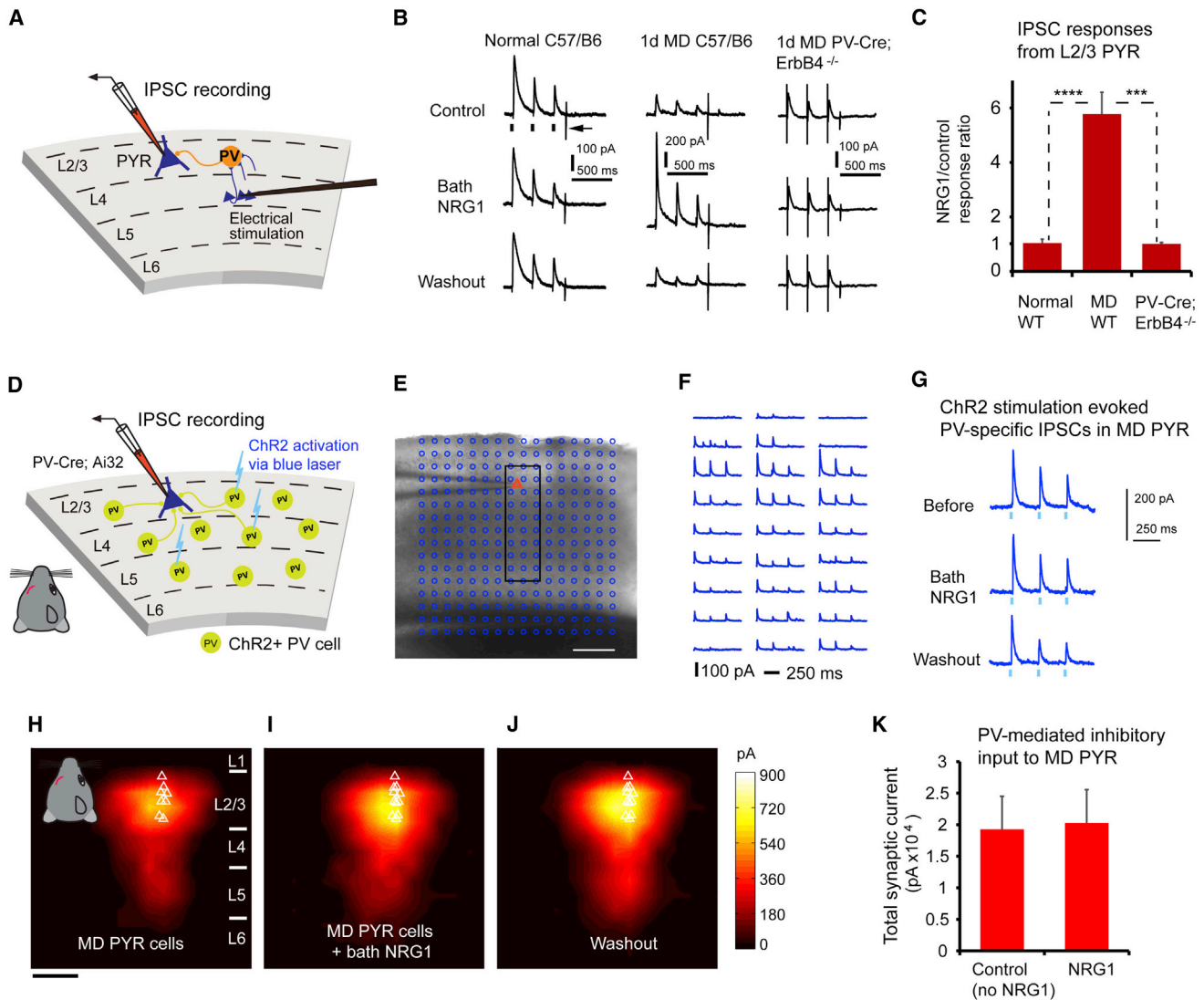


Figure 7. During Critical Period Monocular Deprivation, NRG1 Enhances Evoked Synaptic Inhibition onto Pyramidal Neurons without Altering the Strength of PV Inhibitory Synaptic Connections to Pyramidal Neurons

(A) Schematic of recording inhibitory postsynaptic current (IPSC) responses in L2/3 pyramidal (PYR) neurons by preferentially activating L4->L2/3 feedforward projections to L2/3 PV neurons through L4 electrical stimulation.

(B and C) Bath NRG1 increases evoked IPSCs to monocular-deprived (MD) pyramidal neurons in slices of wild-type C57/B6 mice ($n = 16$ cells), but not normal pyramidal neurons ($n = 6$ cells) or pyramidal neurons ($n = 5$ cells) in slices of PV-Cre; ErbB4^{flx/flx} mice. For each trial, electrical stimulation (1 ms, 20 μ A) was applied three times represented by three black ticks beneath one example trace in (B). For the example trace, the arrow indicates the current injection response to monitor access resistance during the experiment. $***p = 0.003$ and $****p = 6.1E-04$ (Mann-Whitney U tests).

(D–K) The responsiveness of PV inhibitory input connections to deprived pyramidal neurons is not modulated by bath NRG1, as assessed with optogenetically evoked PV inhibitory inputs. (D) Schematic of mapping PV inhibitory IPSCs to individually recorded L2/3 pyramidal neurons in local V1 circuits in PV-Cre; Ai32 mouse slices. (E and F) A representative mapping grid with ChR2 photoactivation sites (cyan circles) is superimposed to the slice image, and ChR2-evoked IPSC responses from the rectangular region in (E) to the recorded pyramidal neuron (red triangle) are shown in (F). (G) Example IPSC responses recorded from the pyramidal neuron shown in (E) while directly activating ChR2-expressing PV cells through optogenetic stimulation in one map location before, during, and after washout of bath NRG1. The repeated blue laser flashes (0.25 ms) represented by three blue ticks beneath the traces in (G) were applied to each map location. Group-averaged, inhibitory input maps of L2/3 pyramidal neurons are shown for (H) before ($n = 11$ cells) and (I) during bath NRG1 (20 min after NRG1 application) and (J) after washout of bath NRG1. White triangles represent individual pyramidal neurons. Color scale (J) indicates integrated PV inhibitory input strength (black = low, yellow = high). (K) Summary data of average total synaptic input strength measured for deprived L2/3 pyramidal neurons ($n = 11$) for control and bath NRG1. There is no significant difference between the groups ($p = 0.7$, Mann-Whitney U test). In (C) and (K), the error bar represents the SEM. The spatial scale bars in (E) and (H) indicate 200 μ m.

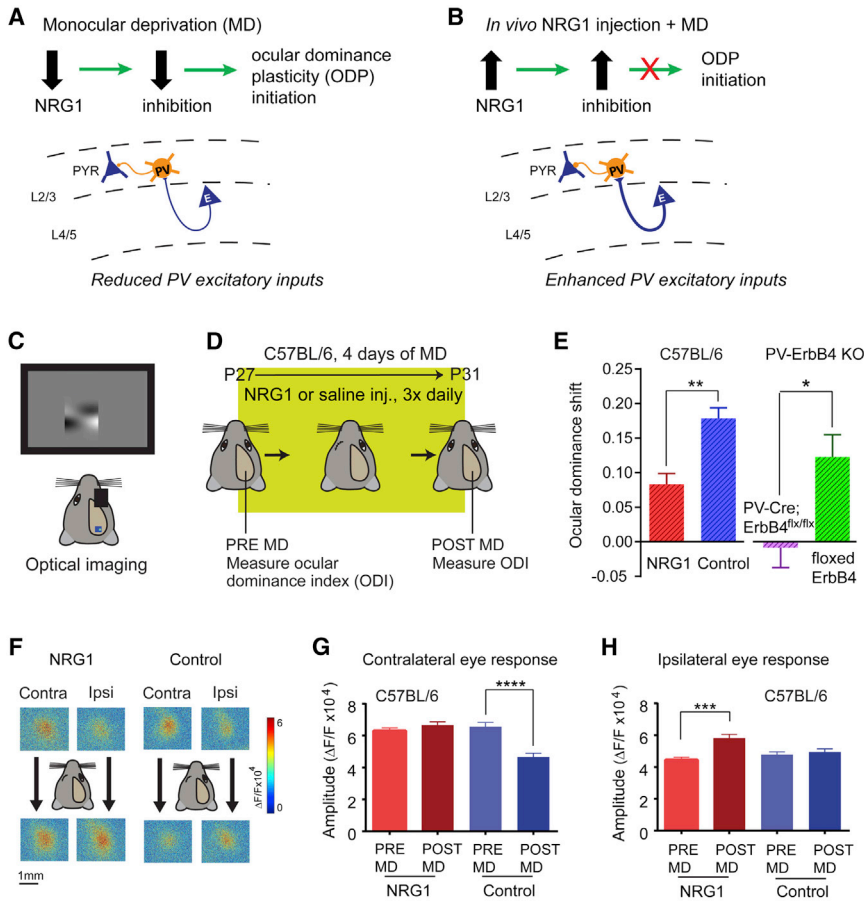


Figure 8. Alteration of NRG1/ErbB4 Signaling in PV Neurons In Vivo Suppresses Critical Period Ocular Dominance Plasticity (A and B) Schematic of our model. (A) Monocular deprivation (MD)-induced reduction of NRG1 expression and NRG1/ErbB4 signaling in PV neurons reduces excitatory inputs onto these cells. The subsequent decrease of cortical inhibition is the necessary first step in ocular dominance plasticity (ODP) initiation. (B) Elevated NRG1 in the cortex enhances excitatory inputs to PV neurons during MD, which occludes the MD-induced reduction of cortical inhibition and suppresses ODP during the normal critical period.

(C–E) The reduction in ocular dominance shift observed after NRG1 treatment during the critical period reflects a suppression of ODP. Illustration of the experimental paradigm (C and D) for assessing ocular dominance in wild-type C57BL/6 mice before and after 4 days of MD during the critical period. (E) Ocular dominance shift is reduced in NRG1-treated critical period animals ($n = 6$, red) compared with control critical period animals ($n = 7$, blue). $**p = 0.004$ (Mann-Whitney U test). Plasticity is also reduced in PV-specific ErbB4 knockout (KO) animals (PV-Cre; ErbB4^{flx/flx}, $n = 6$, purple) compared with their ErbB4^{flx/flx} littermates ($n = 8$, green). $*p = 0.014$ (Mann-Whitney U test).

(F) Examples of contralateral and ipsilateral visual response maps from an NRG1-treated animal (left) and a control animal (right) before (top panels) and after (bottom panels) 4 days of MD. While deprivation causes a loss of contralateral deprived eye input in normal mice, it causes non-deprived ipsilateral eye gain in NRG1-treated animals.

(G), Contralateral (deprived) input changes for control: pre-MD ($n = 7$ mice, 24 responses) versus post-MD ($n = 7$ mice, 23 responses). $****p = 0.0001$ (Mann-Whitney U test). No contralateral input change observed in NRG1 treated animals: pre-MD ($n = 7$ mice, 22 responses) versus post-MD ($n = 5$ mice, 16 responses). $p = 0.3$ (Mann-Whitney test).

(H) In contrast, ipsilateral input increases in NRG1-treated animals: pre-MD ($n = 6$ animals, 18 responses) versus post-MD ($n = 6$ mice, 15 responses). $***p = 0.0002$ (Mann-Whitney U test). No ipsilateral input change observed in control animals: pre-MD ($n = 6$ animals, 23 responses) versus post-MD ($n = 6$ animals, 23 responses). $p = 0.6$ (Mann-Whitney test). In (E)–(H), the error bar represents the SEM.

signaling following visual deprivation reduces excitatory inputs to PV neurons and subsequent inhibition onto excitatory neurons. Considering that enhancing inhibition prevents ocular dominance plasticity during the critical period (Kuhlman et al., 2013; Ma et al., 2013), we tested the hypothesis that enhancing NRG1/ErbB4 signaling in the cortex through systemic NRG1 administration will suppress ocular dominance plasticity (Figure 8B). To measure this plasticity, we determined the strength of eye-specific visual responses before and after 4 days of monocular deprivation using intrinsic signal optical imaging (Davis et al., 2015; Kalatsky and Stryker, 2003; Southwell et al., 2010) (Figures 8C and 8D). We assessed ocular dominance shifts in wild-type C57BL/6 mice treated subcutaneously with NRG1 versus saline following deprivation. In support of our hypothesis, the enhancement of NRG1 signaling (verified by post hoc immunostaining) strongly reduces ocular dominance plasticity (Figure 8E, left). To further test the role of ErbB4 signaling in ocular dominance plasticity, we performed imaging experiments before and after 4 days of monocular deprivation (without NRG1 treat-

ment) using the PV-Cre; ErbB4^{flx/flx} mice and found that critical period plasticity is impaired in animals with PV-specific ablation of ErbB4 receptors (Figure 8E, right).

A hallmark of ocular dominance plasticity during the critical period is the selective reduction of deprived eye visual cortical responses. Enhanced NRG1 signaling blocks the reduction of deprived eye responses that typifies critical period plasticity (Figures 8F and 8G). Further, we find that enhanced NRG1 signaling facilitates a gain of non-deprived eye responses (Figure 8H). This resembles the feature of residual plasticity observed in adult animals after prolonged deprivation (Sato and Stryker, 2008; Sawtell et al., 2003).

DISCUSSION

Although physiological aspects of visual cortical ocular dominance plasticity have been widely studied since the initial discoveries of Hubel and Wiesel more than 50 years ago, the description of underlying molecular mechanisms has lagged behind.

Previous studies have identified that signaling through neurotrophins (nerve growth factor and brain-derived neurotrophic factor), insulin-like growth factor-1, transcriptional control by OTX2, maturation of the extracellular matrix, and synapse formation molecules contribute to regulation of visual cortical plasticity during the critical period (Gu et al., 2013; Huang et al., 1999; Pizzorusso et al., 2002; Sugiyama et al., 2008; Tropea et al., 2006). By leveraging our recent discovery that PV inhibitory neuron activity and local excitatory inputs to PV cells are uniquely affected by brief monocular deprivation during the critical period of visual development (Kuhlman et al., 2013), the present study defines a novel and critical role of NRG1/ErbB4 in the initiation of temporally sensitive visual cortical plasticity by establishing the molecular, cellular, and circuit mechanisms of NRG1/ErbB4 signaling actions.

Our study demonstrates how activity-dependent molecular signaling and sensory experience interact to rapidly shape functional circuit connections in the cortex. It is widely accepted that the maturation of inhibitory circuits creates the conditions necessary for synaptic competition during critical period plasticity. But the developmental mechanism within inhibitory neurons that initiates the critical period has proven elusive. Our work provides evidence that supports a potential cell-autonomous mechanism for NRG1/ErbB4 signaling in PV neuron development. We show that PV neurons express the ligand NRG1 and its receptor ErbB4 during visual cortical development and that blocking ErbB4 activation with an ErbB inhibitor AG1478 decreases NRG1 expression in PV neurons. Consistent with the activity-dependent regulation of NRG1 expression elsewhere in the brain (Eilam et al., 1998; Ozaki et al., 2004), we show that monocular deprivation rapidly downregulates NRG1 expression and its downstream signaling in PV neurons within visual cortex. Visually evoked firing rates of PV neurons are reduced by half with 1-day monocular deprivation (Kuhlman et al., 2013). Thus, PV neurons likely interface firing activity to regulation of NRG1 signaling so as to rapidly translate sensory deprivation into their excitatory input synaptic plasticity. To augment our interpretation of activity-dependent control of NRG1/ErbB4 signaling by PV neurons, we have used DREADDs to specifically reduce PV activity *in vivo* for 24 hr. The DREADDs-evoked suppression of PV neuron spiking decreases NRG1 expression and causes a reduction in local excitatory input to targeted PV neurons as seen in 1-day monocular deprivation. Thus, we establish a mechanistic link between downregulation of NRG1/ErbB4 signaling by visual deprivation, and the subsequent reduction in PV cell activity that facilitates ocular dominance plasticity during the critical period. The developmental downregulation in NRG1 signaling after the critical period further supports the notion that NRG1/ErbB4 signaling is critical to the initiation of juvenile ocular dominance plasticity. Our work suggests that therapeutic manipulation of NRG1/ErbB4 signaling may be developed to help treat central vision disorders in children with amblyopia, as well as other critical period disorders.

We also identify a key synaptic and circuit mechanism through which visual deprivation controls AMPA receptor-mediated synaptic inputs to PV neurons and sensory-evoked recruitment of PV cell-mediated inhibition. Exogenous NRG1 rapidly restores normal excitatory drive onto PV cells and enhances cortical inhi-

bition in deprived cortex. Due to the conserved features of cortical organization, the synaptic and circuit mechanisms through which NRG1 regulates cortical inhibition in an experience-dependent fashion are likely generalized across cortical regions. Our findings offer mechanistic insights for previous studies in the hippocampus showing that NRG1 does not alter electrically evoked glutamatergic transmission at Schaffer collateral-CA1 synapses but increases inhibition to CA1 pyramidal cells to suppress induction of long-term potentiation (Chen et al., 2010; Huang et al., 2000). As the extraordinarily large NRG1 potentiation is observed in deprived but not normal PV neurons in critical period visual cortex, we suspect that NRG1 regulates PV neuronal activity in other brain regions during different developmental stages in a varying and state-dependent manner.

In addition, we identify key components of the NRG1 intracellular signaling cascade for potentiation of excitatory inputs to PV neurons. Since NRG1 potentiation of deprived PV neuron responses does not require NMDA receptors, downstream NRG1/ErbB4 signaling modulation of fast excitatory synaptic transmission is coupled to AMPA receptor membrane targeting in PV neurons. Although multiple NRG1/ErbB signaling pathways are known (Iwakura and Nawa, 2013; Mei and Xiong, 2008), further studies are required to elucidate specific intracellular signaling mechanisms in modulating PV neuronal responses in visual cortex. Through intracellular blocking and other experiments, we demonstrate that downstream PKC activation is essential for NRG1/ErbB4 modulation of the AMPA receptor responses and that acute NRG1 enhancement of PV excitatory inputs requires a membrane fusion-dependent exocytosis of AMPA receptors independent of new protein synthesis.

Defects in NRG1/ErbB4 signaling and PV inhibitory neuronal deficits have been identified as schizophrenia risk factors (Lewis et al., 2005; Mei and Xiong, 2008). Increasing evidence supports the idea that schizophrenia is a neurodevelopment disorder (Rapoport et al., 2012). Schizophrenia has a typical age of onset in late adolescence to early twenties (Gogtay et al., 2011). As schizophrenia appears to result from brain developmental defects during defined postnatal temporal windows (Lewis and Levitt, 2002), our discovery linking NRG1/ErbB4 signaling in PV neurons to critical period plasticity provides new insights into the pathology of schizophrenia. PV neuronal dysfunction, and late adolescent and early adult onset of schizophrenia may be temporally contingent on NRG1/ErbB4 signaling defects in the relevant brain regions. Further understanding of NRG1 signaling in shaping cortical development may shed light on developmental and plasticity disorders of the neocortex.

EXPERIMENTAL PROCEDURES

Animals

All experiment procedures and protocols were approved by the Institutional Animal Care and Use Committee of the University of California, Irvine. Unless specified otherwise, the mice were of both sexes between postnatal days 27 and 31 at the time of experimentation. Further details are described in [Supplemental Experimental Procedures](#).

Immunohistochemistry

To stain tissue sections with antibodies, conventional fluorescent immunohistochemistry was performed as described previously (Xu et al., 2010). Further

details including quantitative fluorescence image analysis are described in [Supplemental Experimental Procedures](#).

Purification of mRNA from fs-TRAP Mice, Western Blotting, and qPCR

Please see the details described in [Supplemental Experimental Procedures](#).

Electrophysiology and Laser-Scanning Photostimulation

Electrophysiological recordings and photostimulation via glutamate uncaging were performed as in reference ([Kuhlman et al., 2013](#); [Xu et al., 2016](#)). PV-specific inhibitory connections to excitatory neurons were mapped using laser-scanning ChR2 photoactivation. Further details are described in [Supplemental Experimental Procedures](#).

Transcranial Intrinsic Signal Optical Imaging

Mapping of the primary visual cortex using Fourier intrinsic signal optical imaging was performed through the intact skull ([Davis et al., 2015](#)). Further details are described in [Supplemental Experimental Procedures](#).

Statistical Analyses

All data are reported as mean \pm SEM. When comparing two independent groups, normally distributed data were analyzed using a Student's *t* test. In the case data were not normally distributed, a Mann-Whitney *U* test was used. In the case more than two groups were compared and data were normally distributed, an ANOVA was performed and followed by post hoc comparisons when justified. In other cases, a non-parametric one-way ANOVA Kruskal Wallis test was used and followed by comparisons with Mann-Whitney *U* tests. A *p* value (≤ 0.05) was considered statistically significant.

Sample size *n* was defined as cell number, except in the case of quantitative immunochemical analysis and comparing the ocular dominance shift across treatments; *n* was defined as animal number or group.

SUPPLEMENTAL INFORMATION

Supplemental Information includes Supplemental Experimental Procedures, eight figures, and two tables and can be found with this article online at <http://dx.doi.org/10.1016/j.neuron.2016.08.033>.

AUTHOR CONTRIBUTIONS

Y.S., N.G., Z.D.L., and X.X. performed molecular experiments, viral injection, and animal preparations. T.I. performed electrophysiological recordings. M.F.D. and X.Z. performed in vivo imaging experiments. L.M. helped with experimental design and provided the loxP-flanked ErbB4 mice. C.L. provided the ErbB4 antibody. X.X., T.C.H., Y.S., S.P.G., and M.F.D. analyzed the data, wrote the manuscript, and prepared the figures. X.X. designed and oversaw the project.

ACKNOWLEDGMENTS

We thank Dr. Joshua T. Trachtenberg for his suggestions on this manuscript. This work was supported by NIH grants NS078434 and MH105427 to X.X.; a Searle Scholars award, Klingenstein Fellowship and an NIH grant EY024504 to S.P.G.; and NIH grants GM102965, and GM107405 to T.C.H. This work was also made possible, in part, through access to the confocal facility of the Optical Biology Shared Resource of the Cancer Center Support Grant (CA-62203) at UC, Irvine.

Received: March 30, 2016

Revised: July 17, 2016

Accepted: August 8, 2016

Published: September 15, 2016

REFERENCES

Abe, Y., Namba, H., Kato, T., Iwakura, Y., and Nawa, H. (2011). Neuregulin-1 signals from the periphery regulate AMPA receptor sensitivity and expression

in GABAergic interneurons in developing neocortex. *J. Neurosci.* *31*, 5699–5709.

Bekhtie, M.M., Finkensieper, A., Binas, S., Müller, J., Wetzker, R., Figulla, H.R., Sauer, H., and Wartenberg, M. (2011). VEGF-mediated PI3K class IA and PKC signaling in cardiomyogenesis and vasculogenesis of mouse embryonic stem cells. *J. Cell Sci.* *124*, 1819–1830.

Berardi, N., Pizzorusso, T., Ratto, G.M., and Maffei, L. (2003). Molecular basis of plasticity in the visual cortex. *Trends Neurosci.* *26*, 369–378.

Chen, C., Xu, R., Clarke, I.J., Ruan, M., Loneragan, K., and Roh, S.G. (2000). Diverse intracellular signalling systems used by growth hormone-releasing hormone in regulating voltage-gated Ca²⁺ or K channels in pituitary somatotropes. *Immunol. Cell Biol.* *78*, 356–368.

Chen, Y.J., Zhang, M., Yin, D.M., Wen, L., Ting, A., Wang, P., Lu, Y.S., Zhu, X.H., Li, S.J., Wu, C.Y., et al. (2010). ErbB4 in parvalbumin-positive interneurons is critical for neuregulin 1 regulation of long-term potentiation. *Proc. Natl. Acad. Sci. USA* *107*, 21818–21823.

D'amour, J.A., and Froemke, R.C. (2015). Inhibitory and excitatory spike-timing-dependent plasticity in the auditory cortex. *Neuron* *86*, 514–528.

Davis, M.F., Figueroa Velez, D.X., Guevarra, R.P., Yang, M.C., Habeeb, M., Carathedathu, M.C., and Gandhi, S.P. (2015). Inhibitory neuron transplantation into adult visual cortex creates a new critical period that rescues impaired vision. *Neuron* *86*, 1055–1066.

Eilam, R., Pinkas-Kramarski, R., Ratzkin, B.J., Segal, M., and Yarden, Y. (1998). Activity-dependent regulation of Neu differentiation factor/neuregulin expression in rat brain. *Proc. Natl. Acad. Sci. USA* *95*, 1888–1893.

Fazzari, P., Paternain, A.V., Valiente, M., Pla, R., Luján, R., Lloyd, K., Lerma, J., Marín, O., and Rico, B. (2010). Control of cortical GABA circuitry development by Nrg1 and ErbB4 signalling. *Nature* *464*, 1376–1380.

Feldman, D.E. (2012). The spike-timing dependence of plasticity. *Neuron* *75*, 556–571.

Frey, R.S., Gao, X., Javaid, K., Siddiqui, S.S., Rahman, A., and Malik, A.B. (2006). Phosphatidylinositol 3-kinase gamma signaling through protein kinase Czeta induces NADPH oxidase-mediated oxidant generation and NF-kappaB activation in endothelial cells. *J. Biol. Chem.* *281*, 16128–16138.

Gogtay, N., Vyas, N.S., Testa, R., Wood, S.J., and Pantelis, C. (2011). Age of onset of schizophrenia: perspectives from structural neuroimaging studies. *Schizophr. Bull.* *37*, 504–513.

Gu, Y., Huang, S., Chang, M.C., Worley, P., Kirkwood, A., and Quinlan, E.M. (2013). Obligatory role for the immediate early gene NARP in critical period plasticity. *Neuron* *79*, 335–346.

Hensch, T.K. (2005). Critical period plasticity in local cortical circuits. *Nat. Rev. Neurosci.* *6*, 877–888.

Hippenmeyer, S., Vrieseling, E., Sigrist, M., Portmann, T., Laengle, C., Ladle, D.R., and Arber, S. (2005). A developmental switch in the response of DRG neurons to ETS transcription factor signaling. *PLoS Biol.* *3*, e159.

Huang, Z.J., Kirkwood, A., Pizzorusso, T., Porciatti, V., Morales, B., Bear, M.F., Maffei, L., and Tonegawa, S. (1999). BDNF regulates the maturation of inhibition and the critical period of plasticity in mouse visual cortex. *Cell* *98*, 739–755.

Huang, Y.Z., Won, S., Ali, D.W., Wang, Q., Tanowitz, M., Du, Q.S., Pelkey, K.A., Yang, D.J., Xiong, W.C., Salter, M.W., and Mei, L. (2000). Regulation of neuregulin signaling by PSD-95 interacting with ErbB4 at CNS synapses. *Neuron* *26*, 443–455.

Huber, K.M., Kayser, M.S., and Bear, M.F. (2000). Role for rapid dendritic protein synthesis in hippocampal mGluR-dependent long-term depression. *Science* *288*, 1254–1257.

Iwakura, Y., and Nawa, H. (2013). ErbB1–4-dependent EGF/neuregulin signals and their cross talk in the central nervous system: pathological implications in schizophrenia and Parkinson's disease. *Front. Cell. Neurosci.* *7*, 4.

Kalatsky, V.A., and Stryker, M.P. (2003). New paradigm for optical imaging: temporally encoded maps of intrinsic signal. *Neuron* *38*, 529–545.

- Kuhlman, S.J., Olivas, N.D., Tring, E., Ikrar, T., Xu, X., and Trachtenberg, J.T. (2013). A disinhibitory microcircuit initiates critical-period plasticity in the visual cortex. *Nature* *501*, 543–546.
- Lewis, D.A., and Levitt, P. (2002). Schizophrenia as a disorder of neurodevelopment. *Annu. Rev. Neurosci.* *25*, 409–432.
- Lewis, D.A., Hashimoto, T., and Volk, D.W. (2005). Cortical inhibitory neurons and schizophrenia. *Nat. Rev. Neurosci.* *6*, 312–324.
- Li, Q., Roberts, A.C., and Glanzman, D.L. (2005). Synaptic facilitation and behavioral dishabituation in Aplysia: dependence on release of Ca²⁺ from postsynaptic intracellular stores, postsynaptic exocytosis, and modulation of postsynaptic AMPA receptor efficacy. *J. Neurosci.* *25*, 5623–5637.
- Liu, X., Bates, R., Yin, D.M., Shen, C., Wang, F., Su, N., Kirov, S.A., Luo, Y., Wang, J.Z., Xiong, W.C., and Mei, L. (2011). Specific regulation of NRG1 isoform expression by neuronal activity. *J. Neurosci.* *31*, 8491–8501.
- Livak, K.J., and Schmittgen, T.D. (2001). Analysis of relative gene expression data using real-time quantitative PCR and the 2(-Delta Delta C(T)) Method. *Methods* *25*, 402–408.
- Long, W., Wagner, K.U., Lloyd, K.C., Binart, N., Shillingford, J.M., Hennighausen, L., and Jones, F.E. (2003). Impaired differentiation and lactational failure of ErbB4-deficient mammary glands identify ERBB4 as an obligate mediator of STAT5. *Development* *130*, 5257–5268.
- Lu, W., Man, H., Ju, W., Trimble, W.S., MacDonald, J.F., and Wang, Y.T. (2001). Activation of synaptic NMDA receptors induces membrane insertion of new AMPA receptors and LTP in cultured hippocampal neurons. *Neuron* *29*, 243–254.
- Ma, W.P., Li, Y.T., and Tao, H.W. (2013). Downregulation of cortical inhibition mediates ocular dominance plasticity during the critical period. *J. Neurosci.* *33*, 11276–11280.
- Madisen, L., Zwingman, T.A., Sunkin, S.M., Oh, S.W., Zariwala, H.A., Gu, H., Ng, L.L., Palmiter, R.D., Hawrylycz, M.J., Jones, A.R., et al. (2010). A robust and high-throughput Cre reporting and characterization system for the whole mouse brain. *Nat. Neurosci.* *13*, 133–140.
- Madisen, L., Mao, T., Koch, H., Zhuo, J.M., Berenyi, A., Fujisawa, S., Hsu, Y.W., Garcia, A.J., 3rd, Gu, X., Zanella, S., et al. (2012). A toolbox of Cre-dependent optogenetic transgenic mice for light-induced activation and silencing. *Nat. Neurosci.* *15*, 793–802.
- Maffei, A., Lambo, M.E., and Turrigiano, G.G. (2010). Critical period for inhibitory plasticity in rodent binocular V1. *J. Neurosci.* *30*, 3304–3309.
- Mei, L., and Xiong, W.C. (2008). Neuregulin 1 in neural development, synaptic plasticity and schizophrenia. *Nat. Rev. Neurosci.* *9*, 437–452.
- Ozaki, M., Itoh, K., Miyakawa, Y., Kishida, H., and Hashikawa, T. (2004). Protein processing and releases of neuregulin-1 are regulated in an activity-dependent manner. *J. Neurochem.* *91*, 176–188.
- Pizzorusso, T., Medini, P., Berardi, N., Chierzi, S., Fawcett, J.W., and Maffei, L. (2002). Reactivation of ocular dominance plasticity in the adult visual cortex. *Science* *298*, 1248–1251.
- Rapoport, J.L., Giedd, J.N., and Gogtay, N. (2012). Neurodevelopmental model of schizophrenia: update 2012. *Mol. Psychiatry* *17*, 1228–1238.
- Sato, M., and Stryker, M.P. (2008). Distinctive features of adult ocular dominance plasticity. *J. Neurosci.* *28*, 10278–10286.
- Sawtell, N.B., Frenkel, M.Y., Philpot, B.D., Nakazawa, K., Tonegawa, S., and Bear, M.F. (2003). NMDA receptor-dependent ocular dominance plasticity in adult visual cortex. *Neuron* *38*, 977–985.
- Smith, S.L., and Trachtenberg, J.T. (2007). Experience-dependent binocular competition in the visual cortex begins at eye opening. *Nat. Neurosci.* *10*, 370–375.
- Southwell, D.G., Froemke, R.C., Alvarez-Buylla, A., Stryker, M.P., and Gandhi, S.P. (2010). Cortical plasticity induced by inhibitory neuron transplantation. *Science* *327*, 1145–1148.
- Sternson, S.M., and Roth, B.L. (2014). Chemogenetic tools to interrogate brain functions. *Annu. Rev. Neurosci.* *37*, 387–407.
- Sugiyama, S., Di Nardo, A.A., Aizawa, S., Matsuo, I., Volovitch, M., Prochiantz, A., and Hensch, T.K. (2008). Experience-dependent transfer of Otx2 homeoprotein into the visual cortex activates postnatal plasticity. *Cell* *134*, 508–520.
- Tamura, H., Kawata, M., Hamaguchi, S., Ishikawa, Y., and Shiosaka, S. (2012). Processing of neuregulin-1 by neuropsin regulates GABAergic neuron to control neural plasticity of the mouse hippocampus. *J. Neurosci.* *32*, 12657–12672.
- Tropea, D., Kreiman, G., Lyckman, A., Mukherjee, S., Yu, H., Horng, S., and Sur, M. (2006). Gene expression changes and molecular pathways mediating activity-dependent plasticity in visual cortex. *Nat. Neurosci.* *9*, 660–668.
- Vullhorst, D., Neddens, J., Karavanova, I., Tricoire, L., Petralia, R.S., McBain, C.J., and Buonanno, A. (2009). Selective expression of ErbB4 in interneurons, but not pyramidal cells, of the rodent hippocampus. *J. Neurosci.* *29*, 12255–12264.
- Wen, L., Lu, Y.S., Zhu, X.H., Li, X.M., Woo, R.S., Chen, Y.J., Yin, D.M., Lai, C., Terry, A.V., Jr., Vazdarjanova, A., et al. (2010). Neuregulin 1 regulates pyramidal neuron activity via ErbB4 in parvalbumin-positive interneurons. *Proc. Natl. Acad. Sci. USA* *107*, 1211–1216.
- Woo, R.S., Li, X.M., Tao, Y., Carpenter-Hyland, E., Huang, Y.Z., Weber, J., Neiswender, H., Dong, X.P., Wu, J., Gassmann, M., et al. (2007). Neuregulin-1 enhances depolarization-induced GABA release. *Neuron* *54*, 599–610.
- Xu, X., Roby, K.D., and Callaway, E.M. (2010). Immunohistochemical characterization of inhibitory mouse cortical neurons: three chemically distinct classes of inhibitory cells. *J. Comp. Neurol.* *518*, 389–404.
- Xu, X., Olivas, N.D., Ikrar, T., Peng, T., Holmes, T.C., Nie, Q., and Shi, Y. (2016). Primary visual cortex shows laminar-specific and balanced circuit organization of excitatory and inhibitory synaptic connectivity. *J. Physiol.* *594*, 1891–1910.
- Zhou, P., Zhang, Y., Ma, Q., Gu, F., Day, D.S., He, A., Zhou, B., Li, J., Stevens, S.M., Romo, D., and Pu, W.T. (2013). Interrogating translational efficiency and lineage-specific transcriptomes using ribosome affinity purification. *Proc. Natl. Acad. Sci. USA* *110*, 15395–15400.

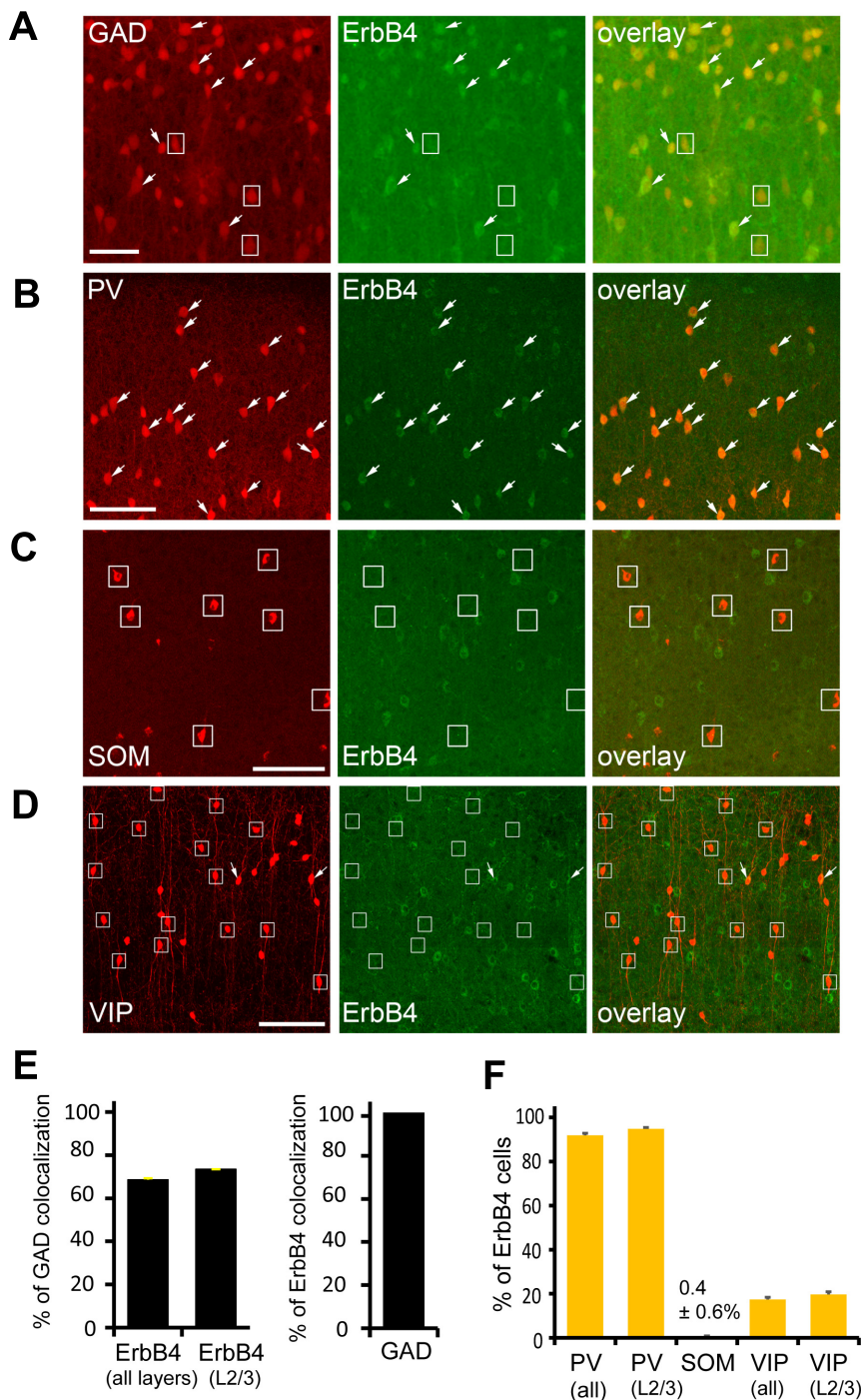
Neuron, Volume 92

Supplemental Information

Neuregulin-1/ErbB4 Signaling

Regulates Visual Cortical Plasticity

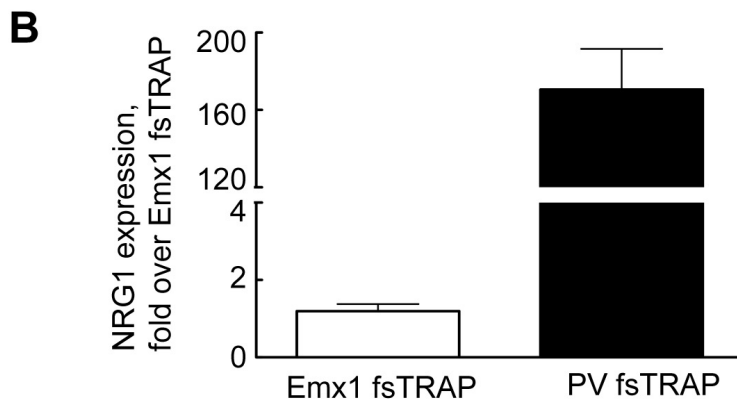
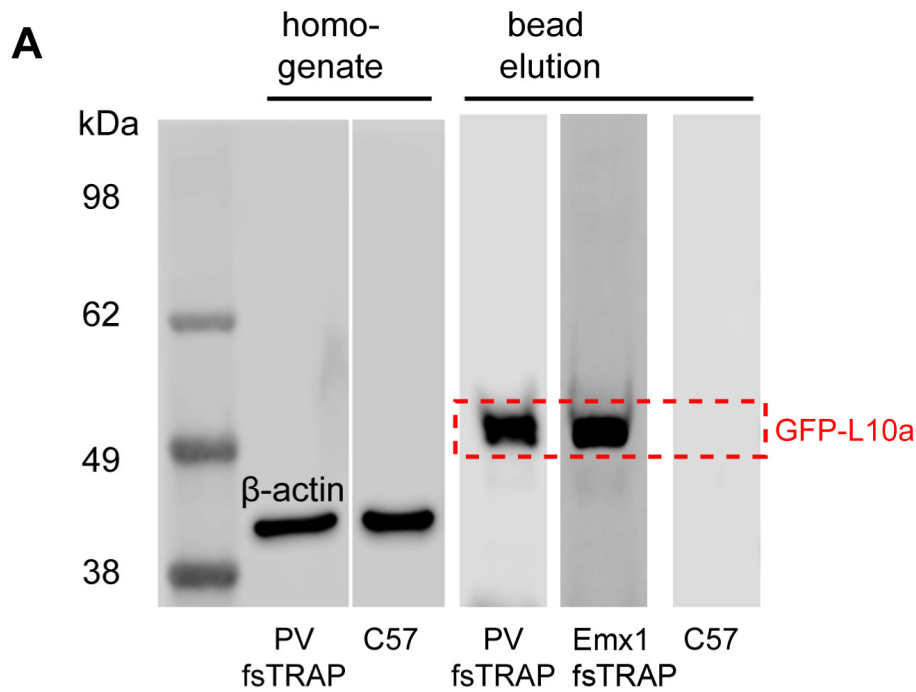
Yanjun Sun, Taruna Ikrar, Melissa F. Davis, Nian Gong, Xiaoting Zheng, Z. David Luo, Cary Lai, Lin Mei, Todd C. Holmes, Sunil P. Gandhi, and Xiangmin Xu



Supplementary Figure 1, related to Figure 1. ErbB4 expression occurs in a subset of GABAergic cells, and is largely restricted to PV neurons in mouse visual cortex during the critical period.

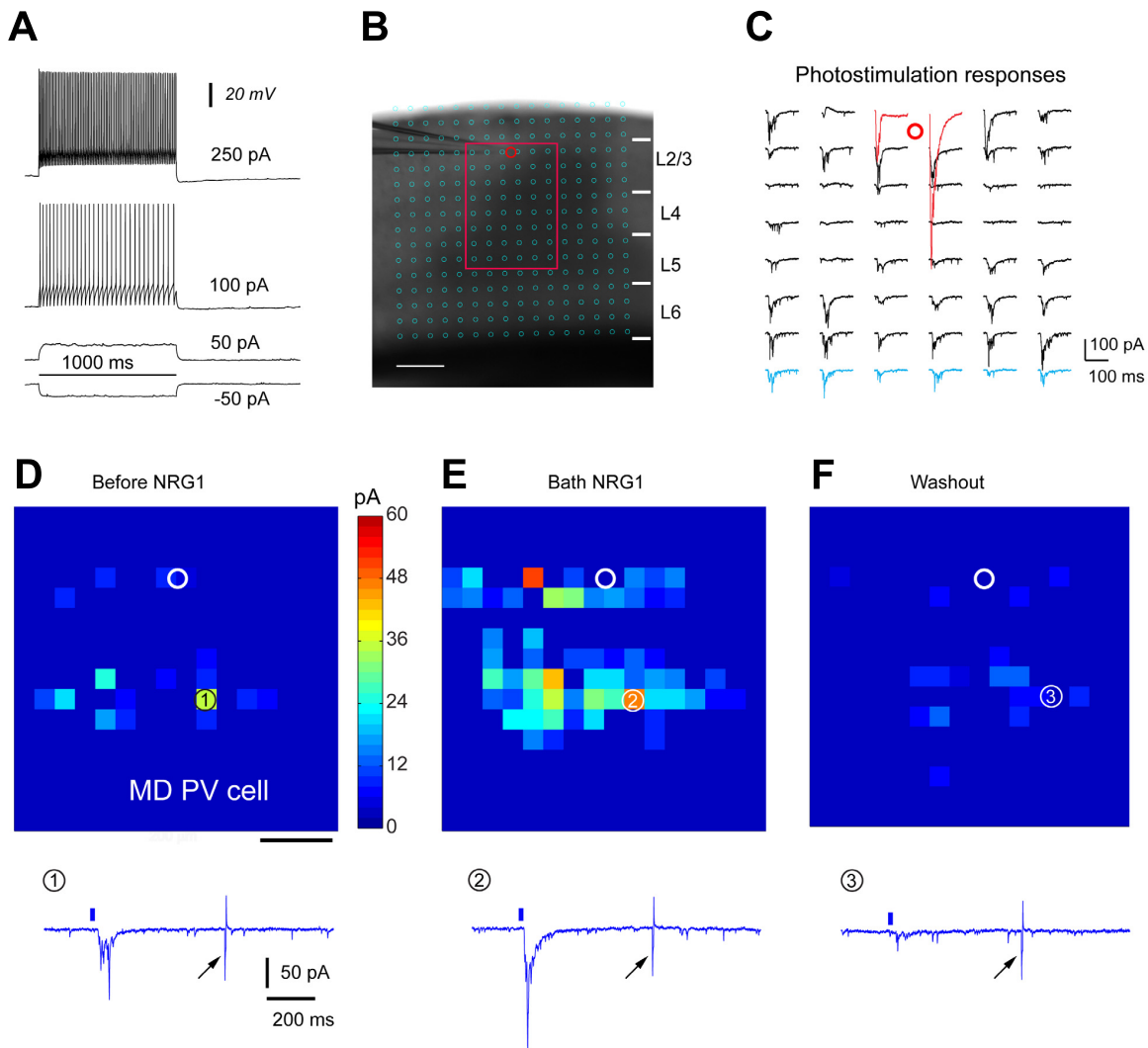
A, Representative confocal images of genetically labeled GABAergic cells (red), ErbB4 immunolabeling (green) and their overlay in layer (L) 2/3 of GAD2-Cre; Ai9 mouse V1. Arrows indicate glutamate decarboxylase (GAD)-expressing cells immunopositive for ErbB4 and white squares encompass ErbB4 immuno-negative GABAergic cells. Scale = 50 μ m. **B**, Representative confocal images of genetically labeled PV cells (red), ErbB4 immunolabeling (green) and their overlay in layer 2/3 of PV-Cre; Ai9 mouse V1. Nearly all PV cells are strongly immunopositive for ErbB4. **C**, Representative confocal images of immunolabeled somatostatin (SOM) cells (red), ErbB4 immunolabeling (green) and their overlay in layer 2/3 of mouse V1. Essentially no SOM cells are immunopositive for ErbB4. **D**, Representative confocal images of genetically labeled vasoactive intestinal peptide (VIP)-expressing cells (red), ErbB4

immunolabeling (green) and their overlay in L2/3 of VIP-Cre; Ai9 mouse V1. A relatively small proportion of VIP cells are immunopositive for ErbB4, indicated with arrows. Scale = 100 μ m in (B, C, D). E, Summary of the quantification of ErbB4 and GAD co-localization. All ErbB4 expressing cells are GAD positive across all cortical layers in mouse V1. Overall, $68.6 \pm 0.73\%$ (mean \pm SEM) of GABAergic cells across all the cortical layers are immunopositive for ErbB4, and $73.4 \pm 0.03\%$ of GABAergic cells in L2/3 are ErbB4 positive. The quantification is based on the counts of 1070 GAD+ cells pooled from 4 sections of 2 different mice. F, Summary of % ErbB4 expressing cells in the subtypes of inhibitory neurons. Overall, $91.9 \pm 1\%$ of PV cells are positive for ErbB4 across all the layers of mouse V1, and in L2/3, $94.8 \pm 0.6\%$ of PV cells are positive for ErbB4. The quantification is based on the counts of 1276 PV cells pooled from 6 sections of 3 different mice. The measurements from 5 sections of 2 different mice indicate that there is virtually no co-localization between SOM and ErbB4, as only 1 out of 344 SOM cells is potentially positive for ErbB4. Overall, $17.4 \pm 1\%$ of VIP cells are positive for ErbB4 across all the layers of mouse V1, and in L2/3, $19.8 \pm 1.2\%$ of VIP cells are positive for ErbB4. The quantification is based on the counts of 283 VIP cells pooled from 3 sections of 2 different mice. The mice for the immunostaining experiments shown in this figure were used between postnatal days of 27 – 29 within the defined critical period. In E and F, the error bar represents the SEM.



Supplementary Figure 2, related to Figure 2. Cell specific fsTRAP analysis indicates that PV neurons in the visual cortex has stronger NRG1 mRNA expression than excitatory neurons targeted by using Emx1-Cre mice.

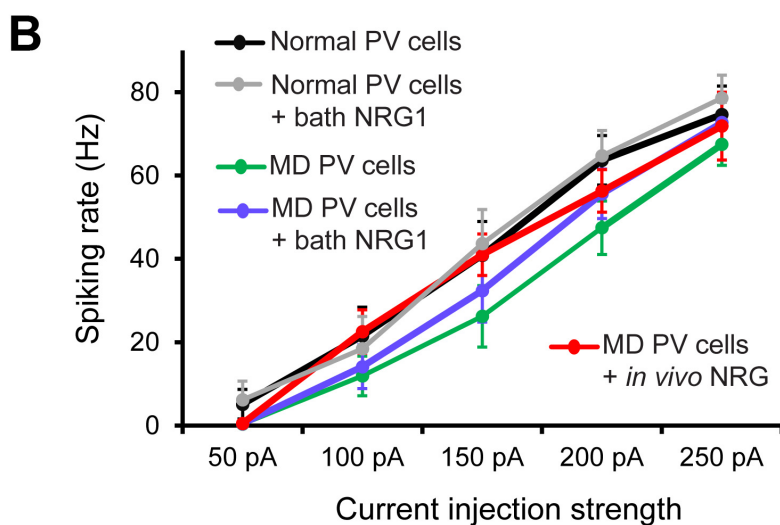
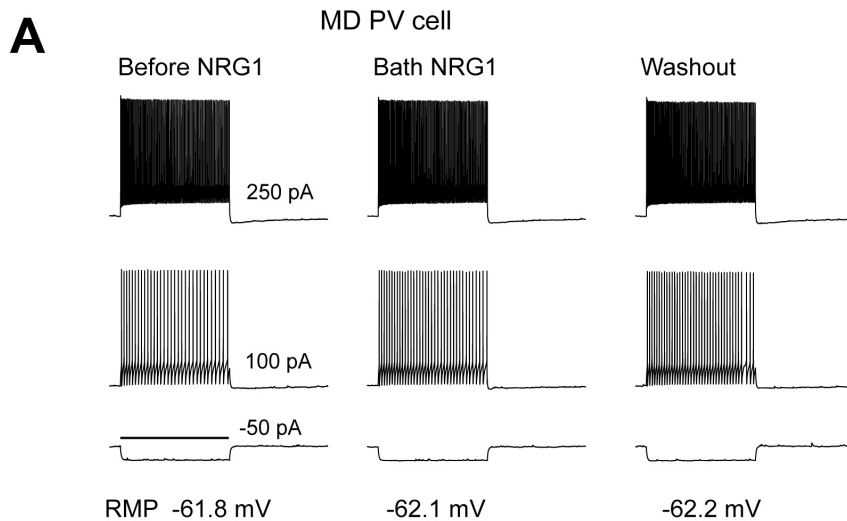
A. Western blotting confirmation of EGFP-L10a tagged polyribosomes in PV-Cre; fsTRAP (PV fsTRAP) and Emx1-Cre; fsTRAP (Emx1 fsTRAP) mice. While both wild type C57/B6 and PV fsTRAP cortical cell-lysate supernatants are positive for β -actin (41 kDa), only the bead elution of PV fsTRAP and Emx1 fsTRAP samples shows immunoblot of EGFP-L10a fusion protein (about 50 kDa in size). This analysis indicates the specificity of Cre-dependent expression of GFP-L10a fusion proteins in fsTRAP cells. **B.** Summary of NRG1 mRNA expression of PV fsTRAP versus Emx1 fsTRAP samples (15 and 9 samples each) using the expression fold over the average Emx1 fsTRAP value. The error bar represents the SEM.



Supplementary Figure 3, related to Figures 3-6. Laser scanning photostimulation (LSPS) allows for quantitative and extensive mapping of local excitatory synaptic inputs to PV neurons.

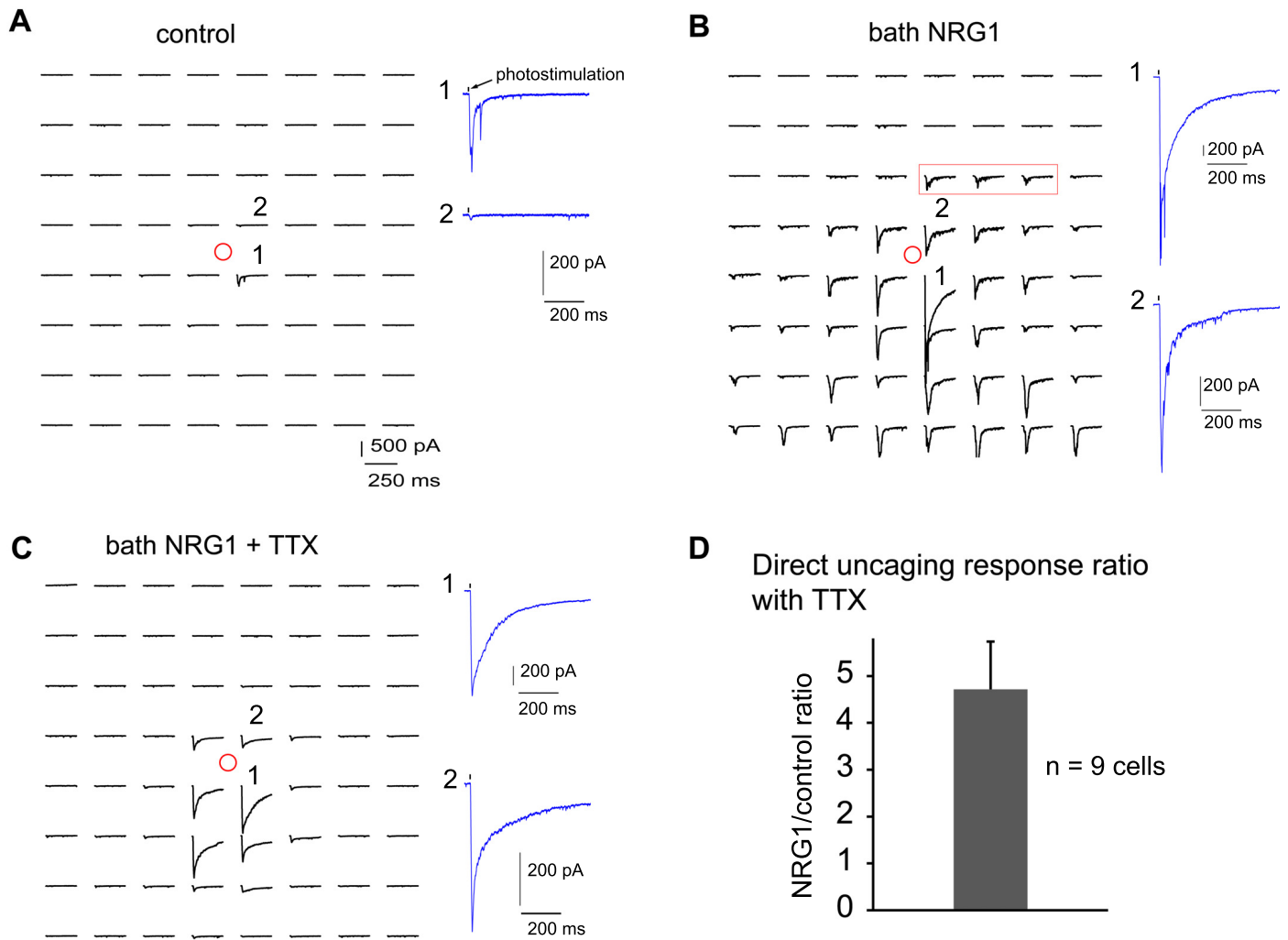
A, PV/fast-spiking (FS) cells are targeted by tdTomato expression in PV-Cre; Ai9 mouse V1 slices, and verified by their typical FS firing patterns evoked by intrasomatic current injections. **B-F**, LSPS allows for extensive and quantitative analysis of synaptic inputs to recorded PV cells from laminar circuits in a relatively large cortical region. **B**, A V1 slice image superimposed with photostimulation sites (cyan circles) spaced at $60\ \mu\text{m} \times 60\ \mu\text{m}$. The red circle indicates the tip of a recording electrode and the cell body location of a recorded L2/3 monocular deprived PV neuron. Scale bar = $200\ \mu\text{m}$. **C**, The plot of excitatory postsynaptic current (EPSC) responses from the recorded PV cell at the selected sites within the region shown by the red rectangle in **B**, in response to photostimulation via glutamate uncaging during NRG1 bath application. The red traces indicate example direct responses, and the blue traces indicate example synaptic input responses. The response traces are plotted for 200 ms beginning at the photostimulation onset. The two types of responses can be distinguished based on their waveforms, amplitudes and response latencies. The direct responses are analyzed for glutamate mediated excitability, but excluded for synaptic input analysis. The raw data as shown in **C** are quantified, and used for construction of color-coded quantitative input maps. **D-F**, Representative example of bath NRG1 enhancement of excitatory synaptic inputs to a deprived PV cell. Data maps were obtained before (**D**), during (**E**) and after washout (**F**) of bath NRG1. The spatial scale beneath (**D**) indicates $200\ \mu\text{m}$. The color scale (**D**) indicates average integrated input strength at individual map sites. The warmer color indicates stronger input strength. The white circle indicates the cell body location of the monocular deprived PV neuron. Each map site (color pixel) is spaced at $60\ \mu\text{m} \times 60\ \mu\text{m}$.

Synaptic input responses at the specified, numbered sites are shown below. The response traces are plotted for 1200 ms, with 200 ms baseline before 1 ms photostimulation (blue ticks above the traces). Arrows indicate current injection responses (5 pA, 5 ms) to monitor access resistance during mapping experiments. Any recordings in which the access resistance changed by >20% during the course of the experiment were excluded from analysis.



Supplementary Figure 4, related to Figure 3. Intrinsic membrane excitability of PV neurons does not change with NRG1 treatment under monocular deprivation or normal conditions.

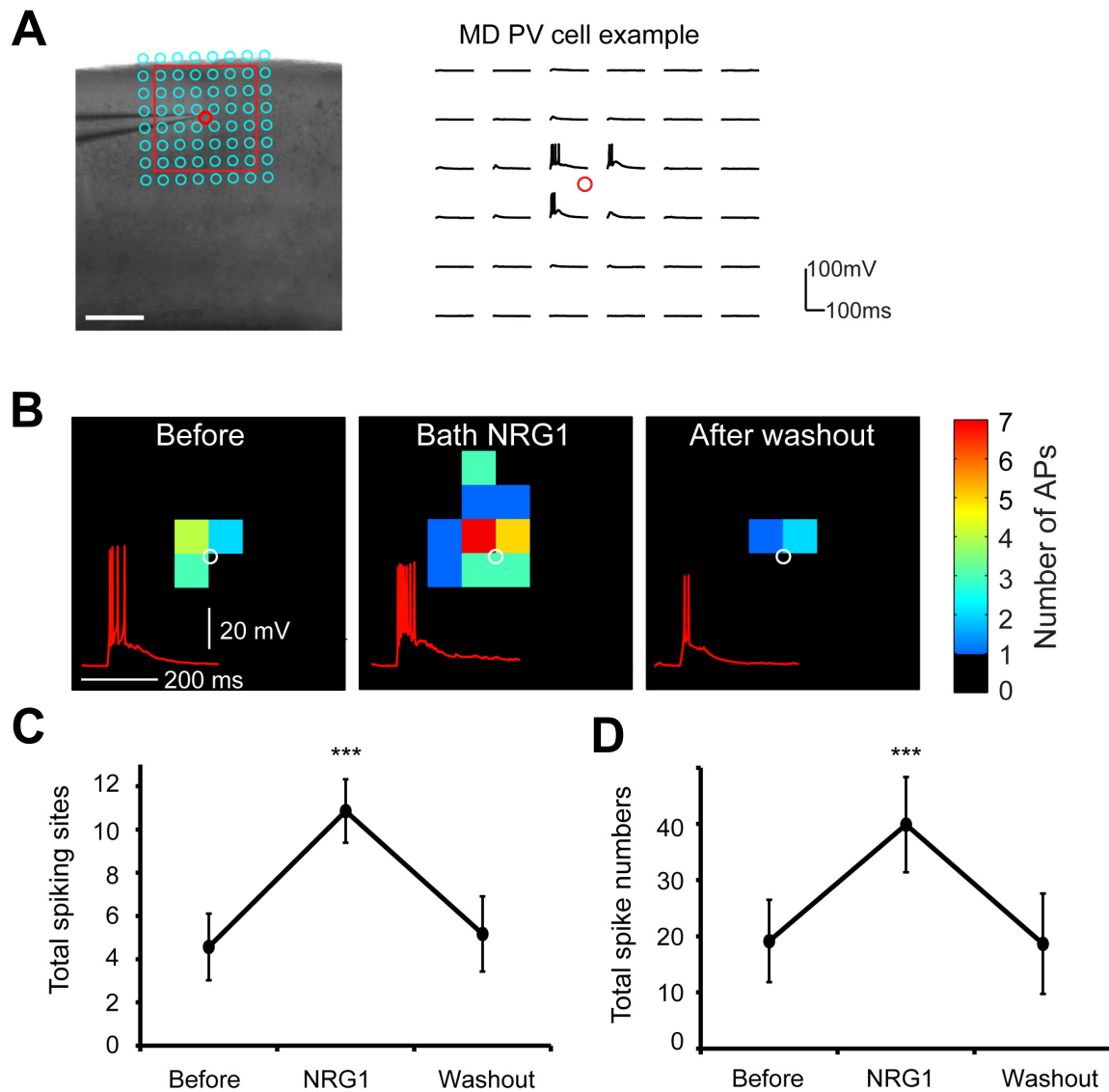
A, Example electrophysiological responses of PV cells from animals subjected to monocular deprivation to depolarizing and hyperpolarizing intrasomatic current injections before, during and after NRG1 bath application. **B**, The plots show the overall relationships between PV cell spiking rates and current injection strengths with the specified conditions. The data values are represented mean \pm SEM, with 14 normal PV cells and 13 deprived PV cells with NRG1 bath application, and 12 deprived PV cells with *in vivo* NRG1 treatment, respectively. There is no significant difference between the plotted data points at each current injection strength.



Supplementary Figure 5, related to Figure 3. NRG1 enhancement of direct uncaging responses of deprived PV neurons persists relative to control with the co-application of tetrodotoxin (TTX) that blocks neuronal action potentials and evoked synaptic inputs.

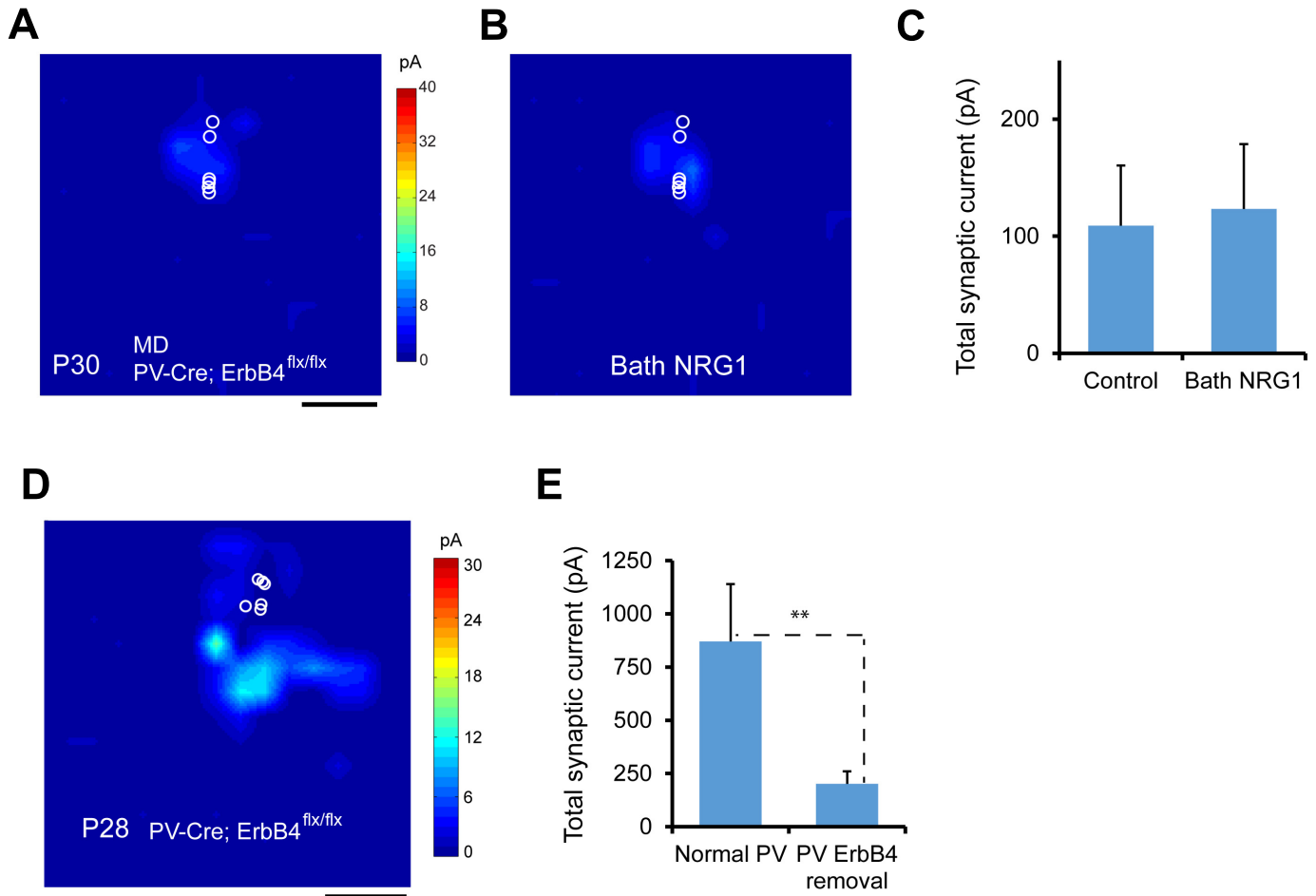
A-C. Example photostimulation data from a deprived PV neuron at control, bath applied NRG1 and the co-application of NRG1 and TTX. The response traces plotted from the photostimulation onset, were acquired from the mapping grid of 8 x 8 sites (65 μm^2 apart), centered at the recorded cell body (indicated by the red circle) at the specified conditions. The responses at the labeled perisomatic sites are expanded and shown separately by the panels. The TTX effect was confirmed by spiking block of the recorded neuron evoked by intrasomatic current injection. Note that the TTX co-application in **C** also blocks evoked synaptic inputs (examples within the red rectangle in **B**) to the recorded neurons.

D. The bar graph shows the average direct uncaging response ratio (4.72 ± 1 , $n = 9$ cells) of before and during bath application of NRG1 and TTX. The error bar represents the SEM.



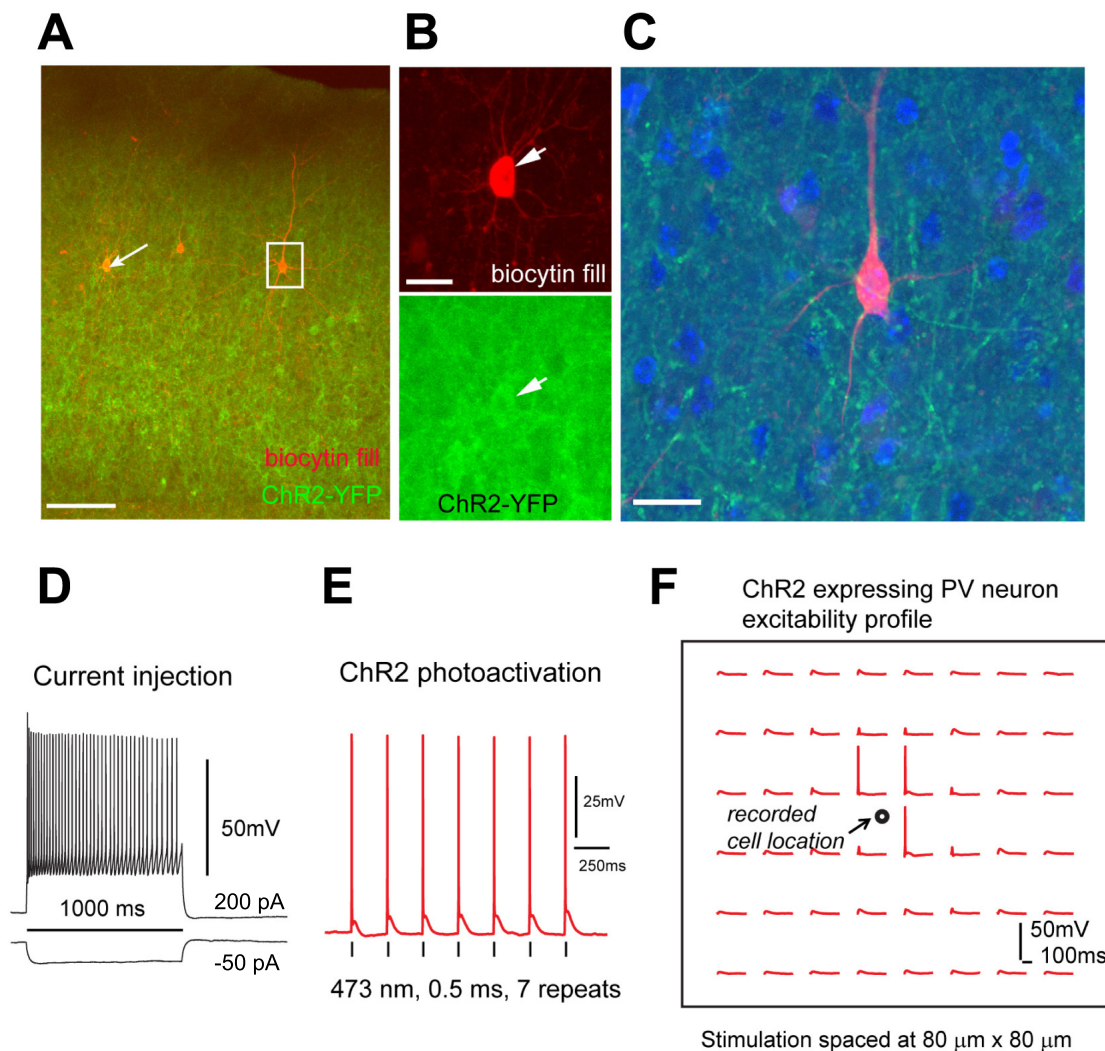
Supplementary Figure 6, related to Figure 3. NRG1 treatment increases glutamate evoked spiking of monocular deprived PV neurons.

A-B, Spiking activities through laser scanning photostimulation via glutamate uncaging are used to assess evoked excitability of PV neurons. **A**, Left: V1 slice image superimposed with photostimulation sites (cyan circles) spaced at $60\ \mu\text{m} \times 60\ \mu\text{m}$. The red circle indicates the tip of a recording electrode and the cell body location of a deprived PV neuron. Right: The plot of photostimulation responses from the recorded PV cells before bath NRG1 at the selected sites within the red square (left). Current clamp recording was used to examine suprathreshold spiking activities in PV neurons. **B**, NRG1 treatment increases glutamate evoked PV neuron excitability in terms of the number of spiking sites and total spike numbers per map, illustrated by the spiking maps recorded before, during and after washout of bath NRG1. The data shown in **(A)** and **(B)** are from the same PV neuron. Each colored square indicates a spiking site. Warmer colors indicate larger numbers of photostimulation evoked action potentials (APs). The inserted traces of spiking are from the uncaging site at the map center under different conditions. **C-D**, Plots of average total spiking sites (**C**) and total spike numbers (**D**) per map for a group of PV cells from monocular deprived animals ($n = 7$ cells) measured before, during and after washout of bath NRG1. Of 7 cells, 6 have complete data and one is lacking washout data. *** indicates the significance level of $p < 0.001$ between NRG1 responses versus baseline or washout (Mann–Whitney U tests). In **C** and **D**, the error bar represents the SEM.



Supplementary Figure 7, related to Figure 6. ErbB4 genetic ablation abolishes NRG1 effects and reduces excitatory synaptic input to PV neurons.

A-C. Bath NRG1 has no effect on deprived PV neurons in PV-Cre^{+/-}; ErbB4^{flx/flx} mice in which ErbB4 is ablated specifically in PV neurons. **A** and **B** show the quantitative group averaged, excitatory input maps before and during bath NRG1 of deprived L2/3 PV neurons (n = 6 cells), respectively. Scale = 200 μ m. **C**, Summary data showing average total synaptic input strength measured from these neurons before and during bath NRG1 (Mann–Whitney U test, p = 0.9). **D-E.** Excitatory synaptic inputs to non-deprived PV neurons from local V1 circuits are reduced in PV-Cre^{+/-}; ErbB4^{flx/flx} mice. **D** shows the quantitative group averaged, excitatory input maps of P28 non-deprived L2/3 PV neurons (n = 6 cells). Scale = 200 μ m. **E**, Summary data showing that average total synaptic input strength measured from ErbB4 knockout PV neurons are weak compared with normal, non-ErbB4 knockout PV cells (n = 11 cells). **, p = 0.02 (Mann–Whitney U test). In **C** and **E**, the error bar represents the SEM.



Supplementary Figure 8, related to Figure 7. Mapping PV-specific inhibitory inputs to excitatory neurons through optogenetic stimulation.

A-C, PV specific ChR2 expression is achieved through a Cre-directed approach by crossing the PV-Cre mouse to the Ai32 mouse with a Rosa-CAG-LSL-ChR2(H134R)-EYFP-WPRE conditional allele. **A**, Confocal image showing yellow fluorescent protein (YFP) fluorescence (i.e., ChR2-fused EYFP expression) (shown in green) of PV cell bodies and their dendrites/axons in a post-fixed PV-Cre; Ai32 mouse slice. The recorded neurons are post hoc identified based on their intrinsic electrophysiology and morphology revealed by intracellular biocytin staining (red). The arrow indicates a PV fast-spiking neuron while the square indicates an excitatory pyramidal neuron. Scale = 100 μ m. **B**, Recording from PV neurons is facilitated by detection of their YFP fluorescence in acutely cut PV-Cre; Ai32 mouse slices. **C**, The pyramidal neuron and many other neurons (revealed by DAPI staining, blue) are surrounded by YFP positive, PV specific axonal processes. Scale = 20 μ m (**B**, **C**). **D-E**, Responses to intrasomatic current injections (**D**) and photoactivation (**E**) (473 nm laser, 3 mW) of a ChR2-expressing PV neuron, respectively. **F**, The excitability profile of the ChR2+, PV neuron to photoactivation (0.25 ms, 3 mW) at the 6 x 8 sites (spaced at 80 μ m²) with 3 spiking sites close to the cell body location, which demonstrates good spatial precision of optogenetic stimulation under our experimental condition. The response traces are plotted for 200 ms beginning at photoactivation onset.

Supplementary Table S1, related to Figure 3 and Supplementary Figure 4. Basic intrinsic properties of normal and deprived PV neurons examined before and during bath NRG1

		Number of neurons	Resting membrane potential (mV)	Input resistance (M Ω)	Rheobase (current strength, pA)	Spike height (mV)
Normal PV neurons	Control	16	-65 \pm 1.1	185.9 \pm 17.3	104.7 \pm 13.9	89.7 \pm 2.8
	NRG1	12	-65.4 \pm 1.2	186 \pm 22	102.1 \pm 19	87.1 \pm 3.3
Deprived PV neurons	Control	14	-62.9 \pm 1.1	180 \pm 9	114.3 \pm 14	95.2 \pm 2.5
	NRG1	13	-63 \pm 1.2	183.2 \pm 8.5	111.5 \pm 14.3	94 \pm 2.9

Supplementary Table S2, related to Figure 3. NRG1 treatment enhances EPSC inputs to deprived PV neurons in terms of the number of detected EPSCs and their integrated amplitudes

	Pre-NRG1 control		Bath NRG1	
	average number of detected EPSCs	average integrated amplitude per EPSC (pA/ms)	average number of detected EPSCs	average integrated amplitude per EPSC (pA/ms)
Normal PV neurons	148 ± 41.8	6.14 ± 0.43	140 ± 38	6.7 ± 0.54
MD PV neurons	50 ± 15.3	5.3 ± 0.43	156 ± 39.5 *	6.91 ± 0.61 *

	Repeated injection for 48 hours		single injection, 1 hour	
	average number of detected EPSCs	average integrated amplitude per EPSC (pA/ms)	average number of detected EPSCs	average integrated amplitude per EPSC (pA/ms)
MD PV neurons with <i>in vivo</i> NRG1 treatment	281.7 ± 46 ***	7.56 ± 0.41 ***	619.3 ± 148 ***	7.13 ± 0.36 *

The quantification listed in this table is related to the analysis shown in Fig. 3J of average total synaptic input strength measured for L2/3 PV neurons under the specified conditions. * indicates the significance of $p < 0.05$ while compared to control data of monocular deprived (MD) PV neurons without NRG1 treatment, and *** indicates the significance of $p < 0.001$.

Supplemental Experimental Procedures

Animals

All experiment procedures and protocols were approved by the Institutional Animal Care and Use Committee of the University of California, Irvine. To genetically label parvalbumin-positive neurons, PV-IRES-Cre knock-in mice (Jackson Laboratories, West Grove, PA, stock #008069) were crossed with the Ai9 tdTomato reporter knock-in mice directly received from Jackson Laboratory (stock #007905). All experimental mice were hemizygous for both transgenes (PV-Cre; Ai9). Similarly, for immunochemical experiments (Supplementary Fig. 1), GABAergic cells were genetically labeled in GAD2-Cre; Ai9 mice, and inhibitory neurons expressing vasoactive intestinal peptides were labeled in VIP-Cre; Ai9 mice (Taniguchi et al., 2011). To control and compare tdTomato labeled PV cells, we also used a few G42 transgenic mice (Chattopadhyaya et al., 2004) in which most GFP-expressing cells are identified as parvalbumin-positive, fast-spiking basket cells. The NRG1 potentiation effect was similarly observed in deprived PV neurons in both PV-Cre; Ai9 and G42 mice. To enable PV specific mRNA expression analysis, PV-Cre mice were crossed to fsTRAP mice (Zhou et al., 2013) (Jackson Laboratory, stock #022367) to generate PV-Cre^{+/-}; fsTRAP mice, in which translating polyribosomes of PV cells are tagged with EGFP from the GFP-L10 transgene. Similarly, EMX1-Cre mice were crossed to fsTRAP mice for targeting excitatory neurons for fsTRAP analysis. Emx1 is predominantly expressed in forebrain excitatory neurons (Gorski et al., 2002). To generate ErbB4 conditional knockout mice, the mice homozygous for loxP-flanked (flx) ErbB4 alleles (Long et al., 2003) were first crossed with PV-Cre mice. The resulting PV-Cre^{+/-}; ErbB4^{flx/+} mice were then crossed back to the homozygous loxP-flanked ErbB4 mice to produce PV-Cre^{+/-}; ErbB4^{flx/flx} mice. Wild-type C57BL/6 (C57/BL6) mice were obtained from Charles River Laboratories (San Diego, CA). The animals (2-5 per cage) were housed in a vivarium room with a 12-h light/dark cycle with access to food and water ad libitum.

Mice were randomly assigned to either control or monocular deprivation treatment groups. Monocular deprivation was performed under isoflurane/oxygen anesthesia (3% induction and 2% maintenance), antibacterial ointment applied to eyes, lid margins trimmed and one mattress suture (silk 6 or 4-0) was used to bind the upper and lower lids. Any mice showing signs of eye infection or lid separation were removed from the study. To enhance NRG1 signaling *in vivo* in the cortex following multiple-day monocular deprivation, some of the animals received subcutaneous administration (3 times (3x) daily, every 8 hours, 0.5 µg NRG1 per mouse) of recombinant human NRG1-β1 purchased from R&D systems (396-HB-050, 8 kDa, Minneapolis, MN). To compare the effects of bath administered NRG1 versus *in vivo* NRG1 treatment, 1-day monocular deprived mice were with subcutaneously administered recombinant NRG1 (single injection, 1 µg NRG1 per mouse). The animals were killed after one hour of NRG1 injection for electrophysiological experiments. The dosage of *in vivo* NRG1 treatment was determined based on our empirical evidence from electrophysiological experiments (Fig. 3) in conjunction with the relevant information from previous studies (Abe et al., 2011; Bersell et al., 2009).

In order to genetically target and label PV neurons in PV-Cre mice or PV-Cre; ErbB4^{flx/flx} mice, we used Cre-dependent AAV-mediated viral expression of mCherry or hM4D-mCherry in these neurons. Mouse pups at P14 were anesthetized under isoflurane for stereotaxic viral injections. The scalp was retracted and a small burr hole was drilled over the left occipital pole overlying the binocular zone of primary visual cortex (V1). A pulled glass pipette (tip diameter ~ 30 µm) was loaded with the AAV5-DIO-hM4D-mCherry or AAV5-DIO-mCherry (~ 2 x 10¹¹ genome units/ml; UNC Vector Core, University of North Carolina at Chapel Hill) and then lowered into the brain, and a Picospritzer was used to pulse 0.1-0.2 µl virus into the binocular V1 region. The scalp was then sutured shut over the burr hole and the mouse was left for 2 weeks to enable high level mCherry or hM4D-mCherry expression. For DREADDs experiments, clozapine N-oxide (CNO) was injected i.p. (0.3 mg/kg, every 8 hours) to inhibit PV neuronal activity *in vivo* at P28 for 24 hours.

Based on published studies (Ellis et al., 2006; Johns et al., 2003; Nagane et al., 2001) and our control experiments, we chose to use intracerebroventricular (i.c.v.) delivery of an ErbB receptor tyrosine kinase inhibitor AG1478 (Cat. No. 658552, Calbiochem/ EMD Millipore, Billerica, MA) in a sub-toxic dosage for the *in vivo* ErbB blockade experiments. Two micro-liters (μ l) of 10 mM AG1478 dissolved in DMSO was injected via a glass pipette to block ErbB4 activation in the cortex of PV-Cre; Ai9 mice, matching our *in vitro* AG1478 experiments. We injected 2 μ l of DMSO in littermate mice for control. The injection was performed with animals undergoing a short duration of isoflurane anesthesia. We did not observe abnormal behaviors or signs of toxicity after AG1478 injection. Given the reported short half-life of *in vivo* AG1478 (Ellis et al., 2006), we divided the animals and let them survive for two different time points, 6 hours (n = 3 animals) and 20 hours (n = 3 animals) after AG1478 injection. While the 6 hour survival group appeared to have stronger reduction in NRG1 expression than the 20 hour survival group, both groups showed a consistent trend of reduced NRG1 expression relative to controls (n = 6 animals). The 6 and 20 hour data are pooled in the final figure (Fig. 2L) for format consistency with the other figures but the time point data detail is described above.

Immunohistochemistry

For immunochemical staining experiments, animals were deeply anesthetized with Uthasol (sodium pentobarbital, 100 mg/kg, i.p.) and transcardially perfused with 5 ml 0.1M phosphate buffered saline (PBS, pH 7.3–7.4), followed by 25 ml 0.1M PBS containing 4% paraformaldehyde and phosphatase inhibitor (PhosSTOP, 1 tablet for 20 ml, Roche, Switzerland). The brains were removed and left in 4% paraformaldehyde for 6-24 hours, then transferred into 30% sucrose in 0.1M PBS. The brains were sectioned coronally in 25 μ m thickness on a freezing microtome (Leica SM2010R, Germany). Selected mouse V1 coronal sections from bregma -3.40 mm to -3.80 mm were used for immunochemical staining experiments and quantitative analysis. For animals having undergone the treatment of monocular deprivation, sections were taken from the hemisphere contralateral to the deprived eye.

Free-floating sections were rinsed 3-4 times with PBS, and incubated in a blocker solution for 1 hour at room temperature on the shaker. The blocker solution contained 5% normal donkey serum and 0.25% Triton X in PBS. Sections were then incubated with the primary antibody in the blocker solution at the appropriate dilution for 36 hours at 4 °C. After the primary antibody incubation, sections were rinsed thoroughly with PBS (or working buffer: 10% blocker and 90% PBS; 6 times), and incubated with an appropriate secondary antibody in the blocker solutions for 2 hours at room temperature. Once the secondary antibody solution was rinsed off, sections were counterstained with 10 µM 4'-6-diamidino-2-phenylindole (DAPI; Sigma-Aldrich, St. Louis, MO) for 10 minutes to help distinguish cortical laminar structures. Finally, sections were rinsed and wet-mounted, and were directly cover-slipped with the mounting medium Vectashield (H-1000, Vector, Burlingame, CA). Primary antibodies against ErbB4 (Rabbit polyclonal, 0618, provided by Dr. Cary Lai at Indiana University; 1:1000), NRG1 (Rabbit polyclonal, ab27303, Abcam, Cambridge, MA; RRID:AB_2154665; 1:300-1000), phospho-ErbB4 (Rabbit monoclonal, ab109273, Abcam; RRID:AB_10866384; 1:250) and phospho-tyrosine (Rabbit monoclonal, RM111, RevMAb; RRID:AB_2619618; 1:300) were used to examine specific immunochemical signals in primary visual cortex, followed with Alexa Fluor (AF) 488-conjugated donkey anti-rabbit secondary antibody (Jackson ImmunoResearch, West Grove, PA, 1:200) to visualize the staining. Per Abcam technical information, the NRG1 antibody is specific to Type 1 isoforms; its specificity was verified through our immunoabsorption tests. We carried immunoabsorption control experiments by pre-incubating 1:1000 dilution of the NRG1 antibody (ab27303) with the recombinant human NRG1-β1 (R&D systems) (10 µg/ml) overnight first, and then adding the mixed antibody and NRG1-β1 solution for subsequent immunochemical staining procedure. The specificity of ErbB4 and phospho-ErbB4 antibodies was confirmed in PV-Cre; ErbB4^{flx/flx} mouse sections. To identify parvalbumin (PV) positive neurons in wild type animals, the primary goat anti-PV antibody (PVG-213, Swant, Switzerland; RRID:AB_10000345; 1:1000) and the secondary Cy3-conjugated donkey anti-goat antibody (Jackson ImmunoResearch, 1:200) were

used. To identify somatostatin (SOM) positive neurons in cortical slices, the primary rat anti-SOM antibody (MAB354, EMD Millipore/Chemicon, Temecula, CA; RRID:AB_2255365; 1:200) and the secondary Cy3-conjugated donkey anti-rat antibody (Jackson ImmunoResearch, 1:200) were used.

Immunostained sections were examined, and low- and high-power image stacks were acquired by using confocal microscopes (LSM 700 and LSM 780, Carl Zeiss Microscopy, Germany). Image tiles, overlaying, maximum projections, and subset z-stack selections were performed using the Zeiss image processing software. For quantitative fluorescence image analysis, all the sections of staining series were acquired using the same acquisition settings (e.g., laser powers, pinhole sizes, line scan numbers), and the data images were digitally processed in an identical manner. Individual cell fluorescence measurements (immunofluorescence) were performed in final output images using Adobe Photoshop software (CS4 extended version, Adobe Systems, San Jose, CA). L2/3 PV or putative excitatory neurons with clear somata in binocular V1 regions were selected; the cell areas (number of pixels) and their integrated density (whole cell fluorescence intensity) were measured. The background reading of the fluorescence level was determined for each stained V1 section image. Corrected total fluorescence per cell (Burgess et al., 2010) in arbitrary units (a.u.) was calculated in an Excel sheet by applying the measurements obtained from the analyzed cell with the formula: Corrected Total Cell Fluorescence (CTCF) = Integrated Density - (Area of selected cell X Mean fluorescence of background reading). For immunostaining fluorescence quantification, the staining intensities (measured by corrected total fluorescence) of PV and non-PV neurons from individual mice (1-2 sections per mouse) in each group were quantified; the mean values with all examined neurons per each mouse were calculated. Then these mean values were normalized to the specified mean for the control condition or age group in the same staining series. The overall normalized values from different mice were compared across different age groups or conditions (e.g., Figs. 1 and 2).

Purification of mRNA from fs-TRAP mice

Purification of polysomally bound mRNA from visual cortical lysate was performed as described with modifications (Zhou et al., 2013). Briefly, visual cortex was dissected in ice-cold ACSF (in mM: 126 NaCl, 2.5 KCl, 26 NaHCO₃, 2 CaCl₂, 2 MgCl₂, 1.25 NaH₂PO₄, and 10 glucose). Pooled visual cortex from two to three mice was grinded to powder on dry ice, followed with sonication for 5 seconds in ice-cold lysis buffer [20 mM HEPES (pH 7.4), 150 mM KCl, 5 mM MgCl₂, 0.5 mM dithiothreitol, 100 µg/ml cycloheximide (Sigma-Aldrich), protease inhibitors (Roche) and 40 U/ml recombinant RNase inhibitor (Promega, Madison, WI)]. Homogenates were centrifuged for 10 minutes at 2,000x g, 4 °C, to pellet nuclei and large cell debris, and NP40 (Invitrogen, Carlsbad, CA) and DHPC (Avanti Polar Lipids, Alabaster, Alabama) were added to the supernatant at final concentrations of 1% (vol/vol) and 30 mM, respectively. After incubation on ice for 5 minutes, the lysate was centrifuged for 10 minutes at 20,000x g to pellet insoluble material. Two mouse monoclonal anti-GFP antibodies, Htz-GFP19C8 and Htz-GFP19F7 (50 µg each, Memorial Sloan-Kettering Monoclonal Antibody Facility, New York, NY) were added to bind to 375 µl protein G Dynal magnetic beads (Invitrogen). Alternatively, 300 µl of the streptavidin Myone T1 dynabeads were binding to 120 µl 1 µg/µl biotinylated protein L first, then followed with two mouse monoclonal anti-GFP antibodies incubation. After being washed twice with the polysome extraction buffer, the beads were then added to the cell-lysate supernatant, and the mixture was incubated at 4 °C with end-over-end rotation for 30 minutes. The beads were subsequently collected on a magnetic rack and washed four times with high-salt polysome wash buffer [20 mM HEPES (pH 7.4), 350 mM KCl, 5 mM MgCl₂, 1% NP-40, 0.5 mM dithiothreitol and 100 µg/ml cycloheximide]. RNA was eluted from the beads by incubating beads in RLT buffer (Rneasy Micro Kit, Qiagen, Venlo, Netherlands) with β-mercaptoethanol (10 µl/ml) for 5 minutes at room temperature. Eluted RNA was purified using RNeasy Micro Kit (Qiagen) per the manufacturer's instructions including in-column DNase digestion. Immunoprecipitated RNA yield for each sample was approximately 3 ng/µl.

Western blotting

To confirm the specificity of Cre-dependent expression of GFP-L10a fusion protein (Supplementary Fig. 2), the bead elution was subjected to denaturing NuPAGE Tris-acetate gel (Invitrogen) electrophoresis and then electrophoretically transferred to nitrocellulose membranes. Five percent low-fat milk in phosphate-buffered saline containing 0.1% Tween-20 was used to block nonspecific binding for at least 1 hour at room temperature. The mouse monoclonal anti-GFP antibodies (Htz-GFP19C8 and Htz-GFP19F7GFP) in phosphate-buffered saline were incubated with the membranes at 4°C for overnight. The antibody-protein complexes were visualized by chemiluminescent reagents.

Quantitative PCR

Purified RNA (30 ng) was used to produce cDNA with a SuperScript® III First-Strand Synthesis SuperMix Kit for RT-qPCR (Invitrogen) following the manufacturer's instructions. Resulting cDNA was used to perform the quantitative PCR with Platinum SYBR Green qPCR SuperMix (Invitrogen), with 500 nM final concentration of each primer. Cycling and quantitation was performed with ViiA™ 7 Real-Time PCR System (Applied Biosystems, Waltham, MA) using the ViiA™ 7 software v1.2. PCR was carried out for 2 min 50 °C, 5 min 95 °C, 40 cycles (15 seconds for 95°C, 30 seconds for 50°C), followed by a melt curve. Each replicate was assayed in sixplicate. Gene expression was normalized to gapdh and presented as mean ± SEM. The following primers were used: ErBb-4-fwd CATGGCCTTCCAACATGACTCTGG, ErBb-4-rev GGCAGTGATTTTCTGTGGGTCCC; NrG1-I/II-fwd GGCAGTGATTTTCTGTGGGTCCC, NrG1-I/II -rev GGCAGTGATTTTCTGTGGGTCCC; gapdh-fwd TGCCAACATCACCATTGTTGA, gapdh -rev TGCCAACATCACCATTGTTGA. For fold enrichment in TRAP, the target gene was normalized to Gapdh in both input and TRAP fractions [i.e., fold TRAP enrichment = $2^{(\Delta Ct_{\text{target}} - \Delta Ct_{\text{gapdh}})}$].

Electrophysiology and laser scanning photostimulation

Coronal sections of 400 μm were cut from mouse V1 with a vibratome (VT1200S, Leica Biosystems, Buffalo Grove, IL) in sucrose containing ACSF (in mM: 85 NaCl, 75 sucrose, 2.5 KCl, 25 glucose, 1.25 NaH_2PO_4 , 4 MgCl_2 , 0.5 CaCl_2 , and 24 NaHCO_3). For animals having undergone monocular deprivation, sections were taken exclusively from the hemisphere contralateral to the deprived eye. Slices were incubated for at least 30 minutes in normal ACSF (in mM: 126 NaCl, 2.5 KCl, 26 NaHCO_3 , 2 CaCl_2 , 2 MgCl_2 , 1.25 NaH_2PO_4 , and 10 glucose) at 32 °C before transferred into slice recording chambers. Throughout the cutting, incubation and recording, the solutions were continuously supplied with 95% O_2 –5% CO_2 .

Whole cell recordings were performed under a DIC/fluorescent Olympus microscope (BX51WI, Olympus, Japan). Oxygenated ACSF at room temperature was perfused into the slice recording chamber through a custom-designed flow system driven by pressurized 95% O_2 –5% CO_2 (3 PSI) at roughly 2 mL/min. Slices were examined under a 4x objective for proper targeting of either L2/3 PV interneurons that express red fluorescent proteins (RFP), tdTomato or excitatory pyramidal neurons within binocular regions of mouse V1 using landmarks defined in reference (Antonini et al., 1999). To target whole cell recordings, cells were visualized at high magnification (60X objective, 0.9 NA; LUMPlanFI/IR, Olympus). Cell bodies of recorded neurons were at least 50 μm below the surface of the slice. Patch pipettes (4 – 6 $\text{M}\Omega$ resistance) made of borosilicate glass were filled with an internal solution containing (in mM) 126 K-gluconate, 4 KCl, 10 HEPES, 4 ATP-Mg, 0.3 GTP-Na, and 10 phosphocreatine (pH 7.2, 300 mOsm). For the recordings in which IPSCs were measured, potassium was replaced with cesium. Electrodes also contained 0.1% biocytin for post-hoc cell labeling and further morphological identification. Once stable whole-cell recordings were achieved with good access resistance (usually <30 $\text{M}\Omega$), basic electrophysiological properties were examined through hyperpolarizing and depolarizing current injections. For intracellular application experiments of PKC inhibitory peptides (PKC 19-36, Tocris, 10 $\mu\text{mol/L}$ in the internal solution of recording pipettes) and light chains of botulinum toxin

type B (BTX) (List Biological Laboratories, Campbell, CA; 2 μ g/mL in the internal solution), we waited for 15 minutes after the neurons were recorded to allow the respective reagents to infuse into the recorded cells for full effects. For protein synthesis inhibition experiments, slices were pre-incubated in 50 μ M anisomycin (a peptidyl transferase inhibitor, Sigma-Aldrich) (Huber et al., 2000; Ramiro-Cortes and Israely, 2013) for 30 minutes before experiments of bath administrated NRG1. Electrophysiological data were acquired with a Multiclamp 700B amplifier (Molecular Devices, Sunnyvale, CA), data acquisition boards (models PCI MIO 16E-4 and 6713, National Instruments, Austin, TX), and custom modified version of Ephus software (Suter et al., 2010). Data were digitized at 10 kHz. Any recordings in which the access resistance changed by >20% during the course of the experiment were excluded from analysis.

PV inhibitory neurons were targeted based on RFP expression and verified by fast spiking patterns from current injections. Excitatory neurons were selected based upon their pyramidal somata detected under differential interference contrast (DIC) microscopy; they were RFP negative, and showed regular spiking patterns to suprathreshold intrasomatic current injections. Final cell type classification was determined by the combined characterization of RFP expression, electrophysiological and morphological properties of the recorded cells. The morphology of recorded neurons was determined using post-hoc staining. Briefly, brain slices were fixed in 4% paraformaldehyde and transferred to 30% sucrose solution in PBS. Neurons filled with biocytin during recordings were labeled with Alexa Fluor 488-conjugated streptavidin (1:500 dilution; Jackson ImmunoResearch). Slices were also stained for DAPI to identify laminar boundaries. Cell morphology, DAPI labeling, and RFP expression were visualized using an Olympus BX61 epifluorescent microscope and MetaMorph imaging suite (Molecular Devices).

Laser scanning photostimulation (LSPS) was performed through a 4x objective lens. Stock solution of MNI-caged-l-glutamate (Tocris Bioscience, United Kingdom) was added to 20 ml of ACSF for a concentration of 0.2 mM caged glutamate. The cortical slice image, acquired through the 4x objective, was visualized using a high-resolution digital CCD camera, and this

image, in turn, was used to guide and register photostimulation sites. Photostimulation (1.5 ms duration, 15 mW pulses) from a 350nm UV laser generator (DPSS Lasers, Santa Clara, CA) was delivered to the sample, controlled via an electro-optical modulator and a mechanical shutter. Focal laser spots approximated a Gaussian profile with a diameter of ~50-100 μm . Under our experimental conditions, LSPS evoked action potentials were recorded from stimulation locations within $88 \pm 11 \mu\text{m}$ ($n = 16$ cells) of targeted somata of excitatory neurons and occurred within 150 ms post photostimulation. Together with control experiments (Xu et al., 2010), our calibration analysis indicates that LSPS allows for mapping direct synaptic inputs to recorded neurons. Synaptic currents in patched neurons were detected under voltage clamp. By systematically surveying synaptic inputs from hundreds of different sites across a large cortical region, aggregate synaptic input maps were generated for individual neurons. For our mapping experiments, a standard stimulus grid (16 \times 16 stimulation sites, 65 μm^2 spacing) was used to tessellate V1 from pia to white matter. The LSPS site spacing was empirically determined to capture the smallest predicted distance in which photostimulation differentially activates adjacent neurons. Glutamate uncaging was delivered sequentially in a nonraster, nonrandom sequence, following a “shifting-X” pattern designed to avoid revisiting the vicinity of recently stimulated sites (Shepherd et al., 2003). Because glutamate uncaging agnostically activates both excitatory and inhibitory neurons, we empirically determined the excitatory and inhibitory reversal potentials in L2/3 pyramidal cells to properly isolate EPSCs and IPSCs. We voltage clamped PV and pyramidal cells at -70 mV to determine LSPS evoked EPSCs.

Photostimulation induces two forms of excitatory responses: (1) those that result from direct activation of the recorded neuron's glutamate receptors, and (2) synaptically mediated responses (EPSCs) resulting from the suprathreshold activation of presynaptic excitatory neurons. Responses that occur within 10 ms of laser pulse onset were considered direct; these responses exhibited a distinct waveform and occurred immediately after glutamate uncaging (Fig. 3A; Supplementary Fig. 3C). Synaptic currents with such short latencies are not possible because

they would have to occur before the generation of action potentials in photostimulated neurons. Therefore, direct responses were excluded from local synaptic input analysis, but they were used to assess glutamate mediated excitability/responsiveness of recorded neurons. At some locations, synaptic responses were over-riding on the relatively small direct responses, and these responses were identified and included in synaptic input analysis. For data map analysis, we implemented the approach for detection and extraction of photostimulation-evoked postsynaptic current responses described in reference (Shi et al., 2010). LSPS evoked EPSCs were quantified across the 16x16 mapping grid for each cell, and 2 to 4 individual maps were averaged per recorded cell, reducing the likelihood of incorporating noise events in the analysis window. The EPSC input from each stimulation site was the measurement of the sum of individual EPSCs within the analysis window (>10 ms to 160 ms post photostimulation), with the baseline spontaneous response subtracted from the photostimulation response of the same site. The value was normalized with the duration of the analysis window (i.e., 150 ms) and expressed as average integrated amplitudes in picoamperes (pA). The analysis window was chosen because photostimulated neurons fire most of their action potentials during this time. For the color-coded map display, data were plotted as the average integrated EPSCs amplitude per pixel location (stimulation site) (e.g., Supplementary Fig. 3), with the color scale coding input strength. For the group maps obtained across multiple cells (e.g., Fig. 3), the individual cell maps were first aligned by their slice images using laminar cytoarchitectonic landmarks. Then a new map grid was created to re-sample and average input strength at each site location across cell maps; a smooth version of color-coded map was presented for overall assessments. To further quantitatively compare input strength across cell groups or different conditions, we measured the total EPSC inputs across all map sites (total synaptic input strength) for individual cells.

For the experiments that examined the effects of bath application of NRG1, AG1478 and CPP (Tocris Bioscience), the reagent(s) was/were added into the recording solution with specified

concentrations. The drug application for 20 minutes was estimated to produce full effects, while the washout of 30 minutes was considered to remove the added drug from the recording solution.

Laser scanning ChR2 photoactivation

Similar to LSPS, we mapped PV specific inhibitory connections to excitatory neurons using laser scanning ChR2 photoactivation. This was achieved with PV inhibitory cell type-specific optogenetic stimulation. The PV-Cre mouse line is crossed to the Ai32 mouse line (Madisen et al., 2012) that has a conditional allele of Rosa-CAG-LSL-ChR2(H134R)-EYFP-WPRE, to drive ChR2/EYFP fusion protein expression in PV cells. Whole cell recordings were made from layer 2/3 pyramidal neurons in binocular visual cortex of PV-Cre; Ai32 mice; spatial maps of PV cell connectivity strength to each patched pyramidal neuron were derived by systematically stimulating ChR2-expressing PV cells at 16 x 16 different sites arranged in a mapping grid across all cortical layers. Spatially restricted optogenetic activating of ChR2-expressing PV cells was accomplished using a 473 nm blue laser (3 mW, 0.25ms; laser spot diameter, ~50 μ m). During optogenetic stimulation experiments, the ionotropic glutamate receptor antagonists [10 μ M 6-cyano-7-nitroquinoxaline-2,3-dione (CNQX) and 5 μ M CCP] were added to the bath solution to block excitatory synaptic input (GABAergic transmission is unaffected) and to avoid any potential dis-inhibition effects. Because interneurons can be interconnected by electrical synapses, we blocked gap junctions using 100 μ M carbenoxolone. The reagents were purchased from Tocris Bioscience. Whole-cell voltage-clamp recordings were made from the recorded pyramidal neurons to measure ChR2-evoked inhibitory post-synaptic currents at the empirically determined holding potential at +5 mV with cesium-containing internal solution. The data analysis was similar to that described above for LSPS.

We have validated the effectiveness of our approach. Following high ChR2 expression in the cortex of the cross-bred pups (PV-Cre; Ai32), living brain slices were prepared and whole cell recordings were performed from ChR2/YFP-expressing PV cells that exhibited robust photoactivation-evoked spikes to repeated laser flashes (473 nm, 3 mW) (Supplementary Fig. 8).

As ChR2-expressing PV cells only fired action potentials to blue laser photoactivation (0.25 ms, 3 mW) close to their cell bodies, we found that ChR2 photoactivation had sufficient spatial precision for laminar circuit mapping under our calibrated conditions.

For electrical stimulation experiments shown in Fig. 7A-C, we recorded inhibitory post-synaptic current responses from L2/3 pyramidal neurons while a concentric bipolar electrode (FHC Inc., Bowdoin, ME) connected to a stimulus isolator (World Precision Instruments, Inc., Sarasota, FL) was placed in L4 to preferentially activate L4 excitatory projections to L2/3 PV neurons.

Transcranial intrinsic signal optical imaging

We used both wild type C57BL/6 and PV-Cre^{+/-}; ErbB4^{flx/flx} mice. There are technical caveats for using the PV-Cre; ErbB4^{flx/flx} mice for *in vivo* studies. Since PV gene expression starts around 2 weeks postnatally, deletion of the ErbB4 gene in PV cells using the PV-Cre; ErbB4^{flx/flx} crossing does not begin to reduce ErbB4 receptor levels until this developmental time point. Although our circuit mapping experiments shows reduced circuit inputs to L2/3 PV neurons in the visual cortex of PV-Cre; ErbB4^{flx/flx} mice, in this genetic condition, our control experiments indicate that ErbB4 is reduced but not eliminated during the *in vivo* experimental time (4 day MD between P27-P31). In addition, high expression levels of ErbB4 are known in both developing and adult retinas (Bermingham-McDonogh et al., 1996). Thus, genetic knockouts of ErbB4 in the retina of the PV-Cre; ErbB4^{flx/flx} mice may affect the light-activated responses of peripheral retinal neurons. Compromised retinal function would in turn complicate our interpretation of the effects of visual deprivation from *in vivo* imaging experiments. However, no differences in the cortical responses to visual stimulation are observed between PV-specific ErbB4 knockout (PV-ErbB4 KO) mice and their control littermates before monocular deprivation. The overall contralateral cortical responses (in the unit of $\Delta F/F \times 10^4$) in PV-ErbB4 KOs (n = 4) and their control littermates (n = 6) are 1.5 ± 0.28 (mean \pm SEM) and 1.39 ± 0.1 , respectively (p = 0.96, Mann-Whitney U test). The overall ipsilateral cortical responses in PV-ErbB4 KOs and their control littermates are 0.99 ± 0.16 (mean

\pm SEM) and 0.96 ± 0.09 , respectively ($p > 0.99$). Although we find that ocular dominance plasticity is impaired in PV-ErbB4 KOs, these data indicate that ablating the ErbB4 receptors specifically in PV interneurons does not perturb the overall cortical responses up to the age tested (P27).

All mice, with treatments blinded for the operators, were anesthetized with isoflurane in O₂ (2%-3% for induction; 1.5% for surgical procedures; 0.6%-0.9% for imaging). During imaging sessions, anesthesia was supplemented by a single intraperitoneal injection of chlorprothixene (1 - 2.5 mg/kg). Atropine (0.3 - 1 mg/kg) and carprofen (5 mg/kg) were administered subcutaneously to reduce secretions and to provide analgesia, respectively. Body temperature was maintained at 37.5°C using a feedback controlled homeothermic heating pad. For imaging, the skull over right visual cortex was exposed and covered with agarose (1.5% w/V in 1X PBS) and a coverslip. Agarose was sealed using sterile ophthalmic ointment (83% white petrolatum, 15% mineral oil; Rugby Laboratories, Livonia, MI) to prevent drying. Eyelashes were trimmed and a thin coat of silicone oil (30,000 cSt; Dow Corning, Midland, MI) was placed over the eyes for protection during imaging.

A SciMedia THT microscope (Leica PlanApo 1.0X; 3.4 mm x 3.4 mm image area) equipped with an Andor Zyla sCMOS camera was used to collect visual response data. The surface vasculature was visualized using a 530 nm LED light with the camera focused on the cortical surface (LED4D210, Thorlabs, Newton, NJ). For intrinsic signal recording, illumination was changed to 617 nm LED light and the camera was focused ~600 μ m beneath the pial surface. Custom written Matlab (Mathworks, Natick, MA) code was used to acquire images and stream data to the disk.

Visual stimuli were generated by custom-written Matlab code using the Psychophysics Toolbox. The monitor was positioned 25 centimeters from the animal and covered with a color correction gel filter sheet (day blue gel D2-70; Lowel, Hauppauge, NY) to better exploit the spectral sensitivity of mouse vision. A visual sweeping noise stimulus was created by multiplying a band limited (<0.05 cyc/deg; <2 Hz) spatiotemporal noise movie with a one dimensional

Gaussian spatial mask (30 degrees) whose position swept across the monitor every ten seconds. Stimuli were presented on an Asus VG248 monitor (30 cm × 53 cm, 144 Hz refresh rate, 35 cd/m² mean luminance). To generate retinotopic response maps, we presented this visual noise stimulus periodically sweeping from -18 to 36 degrees or from 36 to -18 degree visual field elevation. The screen was centered in front of the animal. To measure ocular dominance responses, visual stimulation was limited to the binocular visual field (-10 degree to +20 degree visual field azimuth). Responses in the visual cortex were measured during stimulus presentation to the contralateral or the ipsilateral eye independently (stimulation of the other eye was prevented by blocking vision with a black plastic occluder). One recording session consisted of a stimulus being presented for 5 minutes to one eye. Sets of recordings were made in both directions 4-6 times per eye for a total of 40-60 minutes.

Maps of amplitude and phase of cortical responses were extracted from optical imaging movies via Fourier analysis of each pixel at the frequency of stimulus repetition (0.1 Hz) using custom written Matlab code. Overall map amplitude was computed by taking the maximum of the Fourier amplitude map smoothed with a 5 x 5 Gaussian kernel. Ocular dominance index (ODI) was computed as $ODI = (C-I)/(C+I)$ where C and I are the averaged map amplitudes calculated for contralateral and ipsilateral visual stimulation respectively. Ocular dominance shift (ODS) was calculated for each animal in the adult MD experiments as $ODS = (\text{post-MD ODI} - \text{pre-MD ODI})$.

References for Supplemental Experimental Procedures

- Abe, Y., Namba, H., Kato, T., Iwakura, Y., and Nawa, H. (2011). Neuregulin-1 signals from the periphery regulate AMPA receptor sensitivity and expression in GABAergic interneurons in developing neocortex. *J Neurosci* 31, 5699-5709.
- Antonini, A., Fagiolini, M., and Stryker, M.P. (1999). Anatomical correlates of functional plasticity in mouse visual cortex. *J Neurosci* 19, 4388-4406.
- Birmingham-McDonogh, O., McCabe, K.L., and Reh, T.A. (1996). Effects of GGF/neuregulins on neuronal survival and neurite outgrowth correlate with erbB2/neu expression in developing rat retina. *Development* 122, 1427-1438.
- Bersell, K., Arab, S., Haring, B., and Kuhn, B. (2009). Neuregulin1/ErbB4 signaling induces cardiomyocyte proliferation and repair of heart injury. *Cell* 138, 257-270.

- Burgess, A., Vigneron, S., Brioudes, E., Labbe, J.C., Lorca, T., and Castro, A. (2010). Loss of human Greatwall results in G2 arrest and multiple mitotic defects due to deregulation of the cyclin B-Cdc2/PP2A balance. *Proc Natl Acad Sci U S A* *107*, 12564-12569.
- Chattopadhyaya, B., Di Cristo, G., Higashiyama, H., Knott, G.W., Kuhlman, S.J., Welker, E., and Huang, Z.J. (2004). Experience and activity-dependent maturation of perisomatic GABAergic innervation in primary visual cortex during a postnatal critical period. *J Neurosci* *24*, 9598-9611.
- Ellis, A.G., Doherty, M.M., Walker, F., Weinstock, J., Nerrie, M., Vitali, A., Murphy, R., Johns, T.G., Scott, A.M., Levitzki, A., *et al.* (2006). Preclinical analysis of the analinoquinazoline AG1478, a specific small molecule inhibitor of EGF receptor tyrosine kinase. *Biochem Pharmacol* *71*, 1422-1434.
- Gorski, J.A., Talley, T., Qiu, M., Puelles, L., Rubenstein, J.L., and Jones, K.R. (2002). Cortical excitatory neurons and glia, but not GABAergic neurons, are produced in the Emx1-expressing lineage. *J Neurosci* *22*, 6309-6314.
- Huber, K.M., Kayser, M.S., and Bear, M.F. (2000). Role for rapid dendritic protein synthesis in hippocampal mGluR-dependent long-term depression. *Science* *288*, 1254-1257.
- Johns, T.G., Luwor, R.B., Murone, C., Walker, F., Weinstock, J., Vitali, A.A., Perera, R.M., Jungbluth, A.A., Stockert, E., Old, L.J., *et al.* (2003). Antitumor efficacy of cytotoxic drugs and the monoclonal antibody 806 is enhanced by the EGF receptor inhibitor AG1478. *Proc Natl Acad Sci U S A* *100*, 15871-15876.
- Long, W., Wagner, K.U., Lloyd, K.C., Binart, N., Shillingford, J.M., Hennighausen, L., and Jones, F.E. (2003). Impaired differentiation and lactational failure of Erbb4-deficient mammary glands identify ERBB4 as an obligate mediator of STAT5. *Development* *130*, 5257-5268.
- Madisen, L., Mao, T., Koch, H., Zhuo, J.M., Berenyi, A., Fujisawa, S., Hsu, Y.W., Garcia, A.J., 3rd, Gu, X., Zanella, S., *et al.* (2012). A toolbox of Cre-dependent optogenetic transgenic mice for light-induced activation and silencing. *Nat Neurosci* *15*, 793-802.
- Nagane, M., Narita, Y., Mishima, K., Levitzki, A., Burgess, A.W., Cavenee, W.K., and Huang, H.J. (2001). Human glioblastoma xenografts overexpressing a tumor-specific mutant epidermal growth factor receptor sensitized to cisplatin by the AG1478 tyrosine kinase inhibitor. *J Neurosurg* *95*, 472-479.
- Ramiro-Cortes, Y., and Israely, I. (2013). Long lasting protein synthesis- and activity-dependent spine shrinkage and elimination after synaptic depression. *PLoS One* *8*, e71155.
- Shepherd, G.M., Pologruto, T.A., and Svoboda, K. (2003). Circuit analysis of experience-dependent plasticity in the developing rat barrel cortex. *Neuron* *38*, 277-289.
- Shi, Y., Nenadic, Z., and Xu, X. (2010). Novel use of matched filtering for synaptic event detection and extraction. *PLoS ONE* *5*, e15517.
- Suter, B.A., O'Connor, T., Iyer, V., Petreanu, L.T., Hooks, B.M., Kiritani, T., Svoboda, K., and Shepherd, G.M. (2010). Ephus: multipurpose data acquisition software for neuroscience experiments. *Front Neural Circuits* *4*, 100.
- Taniguchi, H., He, M., Wu, P., Kim, S., Paik, R., Sugino, K., Kvitsiani, D., Fu, Y., Lu, J., Lin, Y., *et al.* (2011). A resource of Cre driver lines for genetic targeting of GABAergic neurons in cerebral cortex. *Neuron* *71*, 995-1013.
- Xu, X., Olivas, N.D., Levi, R., Ikrar, T., and Nenadic, Z. (2010). High precision and fast functional mapping of cortical circuitry through a novel combination of voltage sensitive dye imaging and laser scanning photostimulation. *J Neurophysiol* *103*, 2301-2312.
- Zhou, P., Zhang, Y., Ma, Q., Gu, F., Day, D.S., He, A., Zhou, B., Li, J., Stevens, S.M., Romo, D., *et al.* (2013). Interrogating translational efficiency and lineage-specific transcriptomes using ribosome affinity purification. *Proc Natl Acad Sci U S A* *110*, 15395-15400.